water

MDPI

Article

Failure Mechanism and Risk Evaluation of Water Inrush in Floor of Extra-Thick Coal Seam

Min Cao [1,*], Shangxian Yin [1,*], Huiqing Lian [1], Xu Wang [2], Guoan Wang [1], Shuqian Li [3], Qixing Li [4] and Wei Xu [1]

[1] Hebei State Key Laboratory of Mine Disaster Prevention, North China Institute of Science and Technology, Beijing 101601, China; lhuiq345@163.com (H.L.); 15831607103@163.com (G.W.); wadexu.bj@gmail.com (W.X.)
[2] College of Geology and Environment, Xi'an University of Science and Technology, Xi'an 710054, China; jgqsqq0106@163.com
[3] School of Earth Sciences and Surveying Engineering, China University of Mining and Technology, Beijing 100083, China; lsq_cumtb@163.com
[4] Huangyuchuan Coal Mine, National Energy Yili Energy Co., Ltd., Ordos 017000, China; li01067934@163.com
* Correspondence: caomin727@163.com (M.C.); yinshx03@126.com (S.Y.)

Abstract: In this paper, we investigate the evolution characteristics of floor failure during pressured mining in extra-thick coal seams. A mechanical expression relating floor failure depth to seam thickness is established based on soil mechanics and mine pressure theory. The findings reveal a linear relationship between seam thickness and floor failure depth; specifically, as the coal seam thickens, the depth of floor failure increases. To simulate the mining process of extra-thick coal seams, FLAC3D numerical simulation software is utilized. We analyze the failure process, failure depth, and the behavior of water barriers at the coal seam floor under the influence of extra-thick coal seam mining from three perspectives: rock displacement evolution in the floor, stress evolution in the floor, and plastic deformation. Based on geological characteristics observed in the Longwanggou mine field, we establish a main control index system for assessing floor water-inrush risk. This system comprises 11 primary control factors: water abundance, permeability, water pressure, complexity of geological structure, structural intersection points, thickness of both actual and equivalent water barriers, thickness ratio of brittle–plastic rocks to coal seams, as well as depths related to both coal seams and instances of floor failure. Furthermore, drawing upon grey system theory and fuzzy mathematics within uncertainty mathematics frameworks leads us to propose an innovative approach—the interval grey optimal clustering model—designed specifically for risk assessment concerning potential floor water inrush during pressured mining operations involving extra-thick coal seams. This method of mine water inrush risk assessment is applicable for popularization and implementation in mines with analogous conditions, and it holds practical significance for the prevention of mine water damage.

Keywords: extra-thick coal seam; risk assessment; interval grey optimal clustering; water inrush

check for updates

Academic Editor: Kristine Walraevens

Received: 5 January 2025
Revised: 4 February 2025
Accepted: 27 February 2025
Published: 3 March 2025

Citation: Cao, M.; Yin, S.; Lian, H.; Wang, X.; Wang, G.; Li, S.; Li, Q.; Xu, W. Failure Mechanism and Risk Evaluation of Water Inrush in Floor of Extra-Thick Coal Seam. *Water* **2025**, *17*, 743. https://doi.org/10.3390/w17050743

1. Introduction

In the western and northern region of China, coal mines predominantly operate within a fragile ecological environment. Therefore, the organic integration of mine water management and water conservation practices in mining is crucial for exploring the balance between resource development and ecological protection. Floor water damage refers to the phenomenon in which the presence of a confined aquifer beneath a coal seam leads to significant alterations in rock stress distribution due to mining activities. This disruption results in the destruction of the natural equilibrium, thereby diminishing the effective thickness of the floor's water-barrier layer and impairing its ability to block water. Furthermore, secondary fissures that develop as a consequence of failure within both the floor and underlying aquifer contribute collectively to incidents of floor water inrush [1]. For the coalfields in North China, the primary threat of floor water damage arises from the Ordovician limestone aquifer. This aquifer is characterized by well-developed limestone karst features and a high degree of water richness. Additionally, it has undergone multiple stages of tectonic movement, which has intensified the hydraulic connectivity between various aquifers. Consequently, this results in significant mine water inflow and a high frequency of water-inrush incidents, leading to severe challenges for safety production within coal mines [2].

Many researchers have investigated the phenomenon of floor failure following coal mining from various perspectives, including geology, rock mechanics, and soil mechanics [3–5]. The primary research methodologies employed include: similarity simulation, numerical simulation calculations, theoretical analytical computations, and in situ testing [6]. Due to the numerous factors influencing the failure and deformation of floors, coupled with the constantly changing stress conditions during mining operations, theoretical calculation results are frequently subject to bias [7,8]. In situ testing is recognized as the most direct and reliable method for assessing the failure depth of flooring systems. However, due to constraints associated with construction sites, this method imposes stringent requirements on the testing environment and incurs significant costs. Consequently, it is primarily suitable for localized assessments and cannot be widely implemented across an entire mining operation [9,10]. The numerical simulation method is a widely utilized approach for investigating the plastic failure characteristics of bottom plates [11,12]. The numerical simulation method is capable of constructing geological models under various working conditions. Additionally, it can assess the failure modes of rock strata and determine the deformation modulus of rocks [13,14].

As mining operations have extended to greater depths and thicknesses, the hydrogeological conditions within mines have become progressively more complex. Consequently, floor water inrush has emerged as a significant factor impacting mine safety and production. A scientific and rational approach to predicting and evaluating this issue is essential for ensuring safe mining operations [15]. The traditional methods are simple and easy to calculate and have certain advantages in practical application. However, these methods only consider the two factors of aquifer thickness and aquifer water pressure, ignoring other internal factors, and cannot accurately reflect the diversified problems of floor water-inrush risk. In recent years, many scholars have proposed various novel classification verification methods based on mathematical models or artificial intelligence techniques to solve this problem. Shi Longqing et al. utilized the Gray Wolf Optimization Algorithm in conjunction with the Elman Neural Network to forecast the risk of water inrush from the coal seam floor at Hongqi Coal Mine [16]; Zhang et al. selected 10 main control factors from 14 indicators that were believed to affect water inrush, and compared the accuracy of the GRU model, SVM model and BPMN model [17]. Based on the principles of deep learning theory, Zhao Chende et al. developed a predictive model for assessing the risk of floor water inrush by utilizing seven index factors, including unit water inflow and aquifer water pressure [18]. Yin Shangxian et al. developed an interval grey optimal clustering model integrated with a comprehensive control index system for floor water inrush. This model was specifically designed to evaluate the risk of floor water inrush under deep mining conditions characterized by a thick aquitard at Xingdong Mine [19].

In this work, the FLAC3D (Fast Lagrangian Analysis of Continua) software was utilized to simulate the changes in stress distribution, strain development, and plastic zones within the floor during the mining process at the working face. This simulation aims to elucidate the failure process, failure depth, and failure mechanisms related to floor water isolation. The findings provide a foundational basis for technical measures aimed at preventing and controlling floor water issues in comprehensive caving mining operations within confined water layers of extra-thick coal seams. Utilizing grey theory and membership functions from uncertainty mathematics, an interval grey optimal clustering model is proposed. The model adopts the primary control index system of water inrush risk assessment for Longwanggou Coal Mine as its framework. It addresses the complexity and uncertainty associated with the main control factors, mitigates distortions caused by significant differences in physical meaning, dimension, and magnitude among these factors, thereby enhancing the comprehensiveness and accuracy of the evaluation results.

2. Study Area Overview

The Longwanggou mine field is situated 120 km east of Ordos City in the Inner Mongolia Autonomous Region. The region extends approximately 4.3 to 10.8 km from east to west and spans between 4.3 and 7.7 km in width from north to south, covering a total area of 53.06 km^2. The construction scale is designed for an annual capacity of 10.0 Mt/a. The geographic location is illustrated in Figure 1. The coal mining method employed at this site involves a longwall backward strike type, utilizing fully mechanized caving technology for top coal extraction at full height, along with effective roof management strategies. Currently, the NO. 6 coal seam is being mined within the well field; this seam exhibits thicknesses ranging from 18.8 to 28.8 m, with an average thickness of 24.0 m and a burial depth varying between 352 and 395 m. The inclination of the coal seam ranges from flat (0°) to slightly inclined (5.5°), while the mining length of the working face measures approximately 255 m. It should be noted that the upper coal seams—NO. 3, NO. 5, and NO. 6—overlying the top of the working face are not subject to mining activities; similarly, the NO. 9 coal seam located beneath this working face remains unmined as well. The elevation of the coal seam floor is 846.6~858.1 m, which is 24 m below the water level of Austrian limestone water, and the measured pressure of Austrian limestone water is 0.24 MPa. The floor of the working face is 44.5 m away from the Austrian limestone interface, and there are mainly mudstone and sandstone interlayers between them. The comprehensive column diagram of the well field is illustrated in Figure 2.

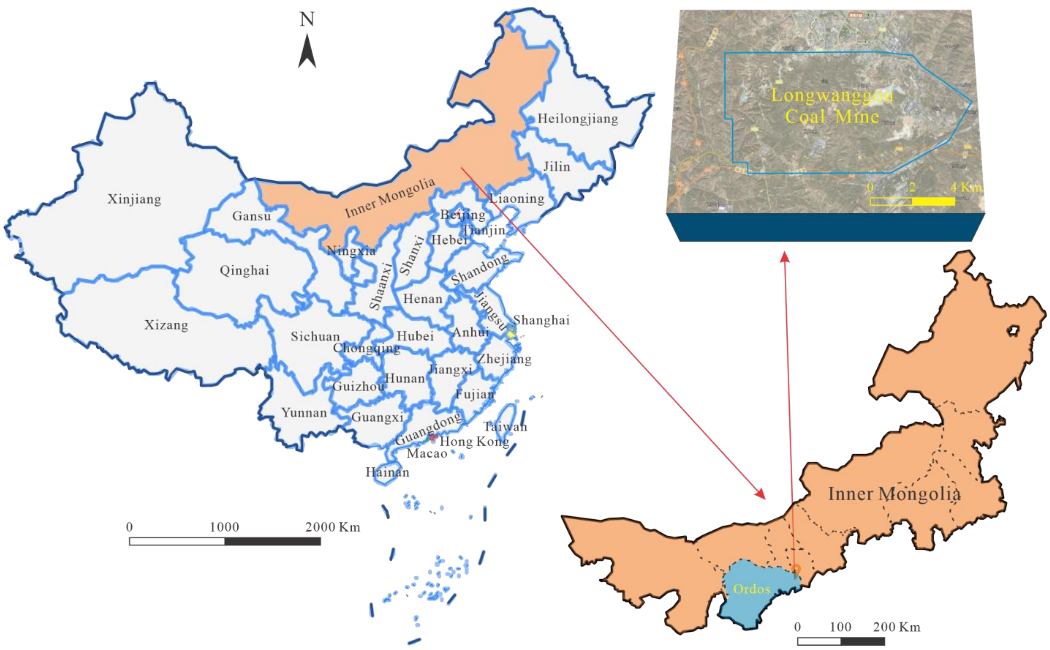

Figure 1. Study area location (China administrative division data from geospatial data cloud).

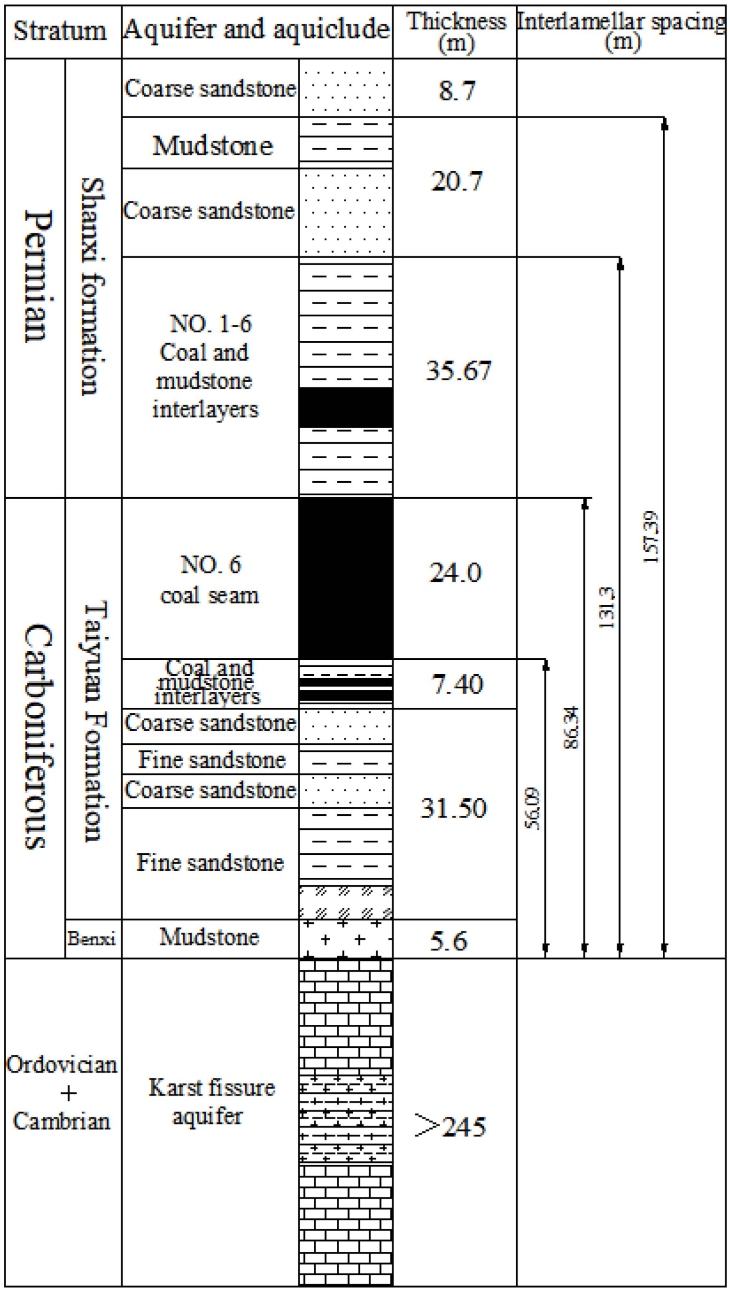

Figure 2. Comprehensive stratigraphic column.

Following the completion of coal mining operations in Longwanggou No. 6, the development height of the water-conducting fracture zone within the overlying strata ranges from 43.56 to 325.29 m. Meanwhile, the vertical distance between the roof of the No. 6 coal seam and the Quaternary loose layer varies from 120.34 to 616.33 m. The calculation results indicate that the water-conduction fracture zone extends into both the upper and lower Shihezi formations, with low-lying areas developing into Quaternary strata and potentially reaching the surface. According to our analysis, the primary direct water source for coal mining at No. 6 is identified as being from the Lower Permian Shanxi Formation aquifer, whereas indirect water sources include aquifers from both upper and lower Shihezi formations as well as those associated with Quaternary sandstone layers. The pore and fissure aquifers affected by the No. 6 coal mining operation generally exhibit moderate recharge conditions with identifiable water supply sources. The unit water inflow of the Shanxi Formation within the Lower Permian system varies from 0.00215 to 0.1841 L/(s·m), indicating overall low water richness, although some localized areas show moderately water-rich characteristics. In contrast, the unit water inflow of the Shihezi aquifer ranges from 0.00212 to 0.02167 L/(s·m), reflecting a weakly water-rich nature. The aquifer within the Quaternary sand layer exhibits a low to moderate water richness. There is an absence of perennial surface water in the area. Additionally, there are no coal mining operations or small kiln mining activities in and around the mine field, which ensures that the mine remains unaffected by goaf water from surrounding mines. Currently, the normal inflow of water into the mine is measured at 55.4 m^3/h, with a maximum recorded inflow of 76 m^3/h. Conversely, another assessment indicates that under different conditions, the normal water inflow can reach up to 168 m^3/h, while its maximum inflow may peak at 258 m^3/h [20].

3. Analysis of Failure Mechanism of Mining Floor of Extra-Thick Coal Seam

3.1. Mechanical Model for the Failure of Coal Seam Floors

Coal seam mining results in the displacement and failure of the underlying rock strata. For direct analysis, the failure pattern is generalized as shown in Figure 3. It can be divided into floor failure zone, transition zone (plastic deformation failure zone) and weathering zone of Ordovician limestone top interface. The failure zone of the floor represents the initial area to experience failure due to abutment pressure following coal mining activities, primarily characterized by shear failure. In the middle transition zone, the stress above the floor is alleviated following the extraction of the coal seam. This results in a significant transformation of the stress state within the floor rock mass, transitioning from a three-dimensional stress condition to either a two-dimensional or unidirectional stress condition [21,22]. The weathering zone at the top interface of Ordovician limestone is formed during the diagenetic process and exhibits relative stability. However, it is generally considered a hazardous area in the context of mine water inrush management due to variations in lithology.

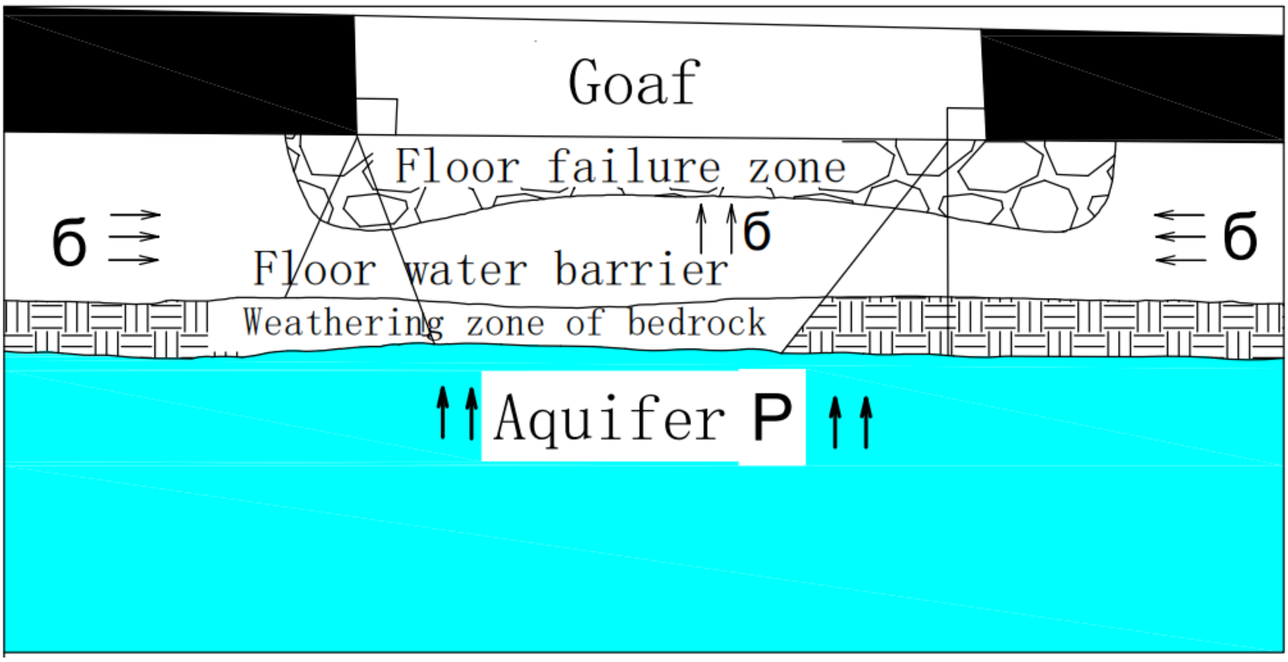

Figure 3. Schematic diagram of floor failure mechanism in mining of extra-thick coal seams over a confined aquifer.

The calculation of floor failure zone can refer to the mature theory of soil mechanics and mine pressure. For the coal body in front of the goaf, a stress element with unit width and thickness as mining height is taken for analysis [23]. The stress state is shown in Figure 4.

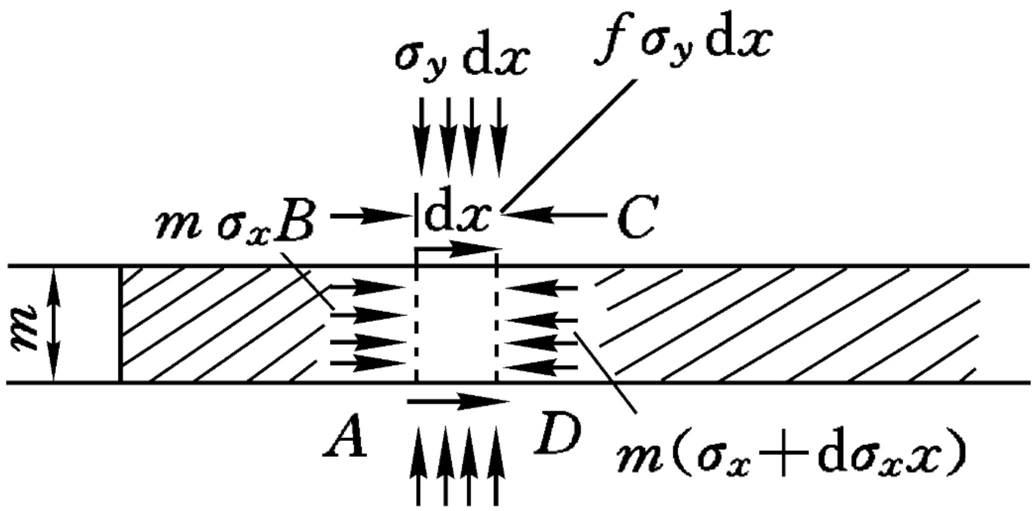

Figure 4. Stress state of limit equilibrium zone.

The thickness of a coal seam is a critical parameter that influences the extent of the limit equilibrium zone. In the horizontal plane, the coal seam located in front of the stope adheres to the limit equilibrium equation as outlined below:

$$m(\sigma_x + d\sigma_x) - m\sigma_x - 2\sigma_y \cdot f \cdot dx = 0 \tag{1}$$

In the formula:

f—coefficient of friction between layers;

m—seam thickness, meter.

According to the Mohr–Coulomb strength criterion, the oblique straight-line strength curve can be expressed in terms of the sum of the ultimate principal stresses. The derivation of this expression is presented as follows:

$$\sigma_x = 2C\sqrt{\frac{1+sin\varphi}{1-sin\varphi}} + \frac{1+sin\varphi}{1-sin\varphi}\sigma_y \tag{2}$$

$$\frac{d\sigma_y}{d\sigma_x} = \frac{1+sin\varphi}{1-sin\varphi} \tag{3}$$

By substituting the above formula into the equilibrium Equation (1) and solving it, we get:

$$ln\sigma_y = \frac{2f \cdot x}{m} \cdot \frac{1+sin\varphi}{1-sin\varphi} + C \tag{4}$$

In the formula, φ is the internal friction angle, °.

Boundary conditions are applied: when $x = 0$, $\partial_y = N_0$, by substituting (1) we get:

$$C = lnN_0 \tag{5}$$

In the formula:

N_0—compressive strength of coal wall, MPa.

By substituting Formula (5) into the limit equilibrium equation, we get:

$$\sigma_y = N_0 e^{\frac{2fx}{m}\frac{(1+sin\varphi)}{(1-sin\varphi)}} \tag{6}$$

Therefore, the width of the limit equilibrium zone of the coal body in front of the working face is:

$$L_{jx} = \frac{m}{2f}\left[\ln(\sigma_y)_{\max} - \ln N_0\right]\frac{1-\sin\varphi}{1+\sin\varphi} \tag{7}$$

In the formula,

$(\sigma_y)_{max}$—Maximum abutment pressure.

It can be observed from soil mechanics that the failure region of the floor is categorized into three distinct areas: the active stress zone, the transitional zone, and the passive stress zone. Notably, the slip line AB within the transition region takes on a logarithmic spiral form, which can be mathematically expressed as follows:

$$l = \frac{L_{jx}}{2cos\left(\frac{\pi}{4}+\frac{\varphi}{2}\right)}e^{\alpha tan\varphi} \tag{8}$$

Referring to the mine pressure theory [24], failure depth of floor formed under abutment pressure D_{max} can be expressed:

$$D_{\max} = \frac{L_{jx}\cdot\cos\varphi}{2\cos\left(\frac{\pi}{4}+\frac{\varphi}{2}\right)}e^{\left(\frac{\pi}{4}+\frac{\varphi}{2}\right)\tan\varphi} \tag{9}$$

By substituting the Formula (7) into the above formula, we get:

$$L = D\frac{m}{4f}\left[ln\frac{(\sigma_y)_{max}}{N_0}\times\frac{(1-sin\varphi)cos\varphi}{(1+sin\varphi)cos\left(\frac{\pi}{4}+\frac{\varphi}{2}\right)}^{\left(\frac{\pi}{4}+\frac{\varphi}{2}\right)tan\varphi}\right]_{max} \tag{10}$$

It can be deduced from the formula that there is a linear correlation between seam thickness and floor failure depth, which constitutes a critical parameter influencing the extent of floor failure.

3.2. FLAC3D Numerical Simulation

The surrounding rock at the working face of Longwanggou Coal Mine predominantly comprises sandstone and shale, which exhibit elastic–plastic material properties. For the calculations, the Mohr–Coulomb yield criterion is utilized:

$$f_s = \sigma_1 - \sigma_3\frac{1+sin\varphi}{1-sin\varphi} - 2c\sqrt{\frac{1+sin\varphi}{1-sin\varphi}} \tag{11}$$

In the formula, σ_1, σ_3 represent the maximum and minimum principal stresses, respectively, c, φ represent the material bonding force and the friction angle. When $f_s \geq 0$, the material is expected to experience failure when subjected to shear stress. After the material reaches the yield limit, plastic deformation occurs at a constant stress level. In a state of tensile stress, if the applied tensile stress surpasses the material's tensile strength, it will result in damage to the material.

3.2.1. Model Building

Based on the comprehensive stratigraphic information from the column diagram of the 61,601 working faces and the adjacent "No. 3 Borehole" and "Guan 8 Borehole", the rock mechanics parameters were determined as presented in Table 1. This determination was made by integrating existing rock mechanics experimental data, the "Engineering Rock Mass Classification Standard", mechanical calculations, empirical formulae, and field measurements. According to the exploration data for the coal seam, its dip angle is confirmed to be less than 8°. Consequently, a numerical model assuming a horizontal coal seam has been established, as depicted in Figure 5. In the Cartesian coordinate system, the X-axis indicates the direction of advance of the working face, whereas the Y-axis signifies its orientation. The Z-axis indicates the vertical orientation of the table. The model dimensions are specified as $X \times Y \times Z = 800$ m $\times$ 600 m $\times$ 520 m, with the distance from the No. 6 coal seam to the Austrian ash layer measuring 44.5 m. The model comprises a total of 417,600 grids and features 434,808 grid nodes.

Table 1. Physical and mechanical parameters of rock formation.

Number	Stratum	Thickness (m)	Cumulative Thickness (m)	Density (kg·m^{-3})	Bulk Modulus (Pa)	Shear Modulus (Pa)	Internal Friction Angle (°)	Cohesive Force (Pa)	Tensile Strength (Pa)
1	Ordovician limestone	80	80	2610	3.50×10^9	2.63×10^9	34.3	1.46×10^6	1.23×10^6
2	Aluminous mudstone	9.6	89.6	2400	2.44×10^9	1.26×10^9	30.6	8.10×10^5	9.30×10^5
3	Mudstone 1	7.5	97.1	2460	2.47×10^9	1.34×10^9	31.3	9.20×10^5	1.14×10^6
4	Coarse sandstone 1	9.7	106.8	2200	2.61×10^9	1.57×10^9	22.5	1.23×10^6	1.23×10^6
5	Sandy mudstone	5.7	112.5	2250	2.20×10^9	1.02×10^9	20.4	9.40×10^5	8.20×10^5
6	Coarse sandstone 2	7.2	119.7	2360	2.52×10^9	1.44×10^9	22.2	1.09×10^6	1.13×10^6
7	6–9 slime Interlayered	4.8	124.5	2450	2.25×10^9	1.10×10^9	23.5	7.00×10^5	7.50×10^5
8	NO. 6 Coal seam	23.8	148.3	1420	1.67×10^9	6.82×10^9	21.6	6.00×10^5	5.00×10^5
9	Mudstone 2	7.3	155.6	2500	2.05×10^9	9.46×10^9	26.8	1.02×10^6	8.40×10^5
10	Coarse sandstone 3	10	165.6	2440	2.96×10^9	1.95×10^9	28.4	8.50×10^5	1.03×10^6
11	Sand–mudstone Interbedded 1	26.9	192.5	2340	2.43×10^9	1.32×10^9	31.1	9.70×10^5	9.10×10^5
12	Coarse sandstone 4	21	213.5	2280	3.16×10^9	2.08×10^9	33.9	9.60×10^5	1.16×10^6
13	Sand–mudstone Interbedded 2	66.3	279.8	2510	2.57×10^9	1.47×10^9	31.7	1.14×10^6	9.20×10^5
14	Coarse sandstone 5	63.8	343.6	2370	2.89×10^9	1.82×10^9	23.2	1.70×10^6	1.34×10^6
15	Top roof	176.4	520	2420	3.49×10^9	2.84×10^9	20.6	1.34×10^6	1.42×10^6

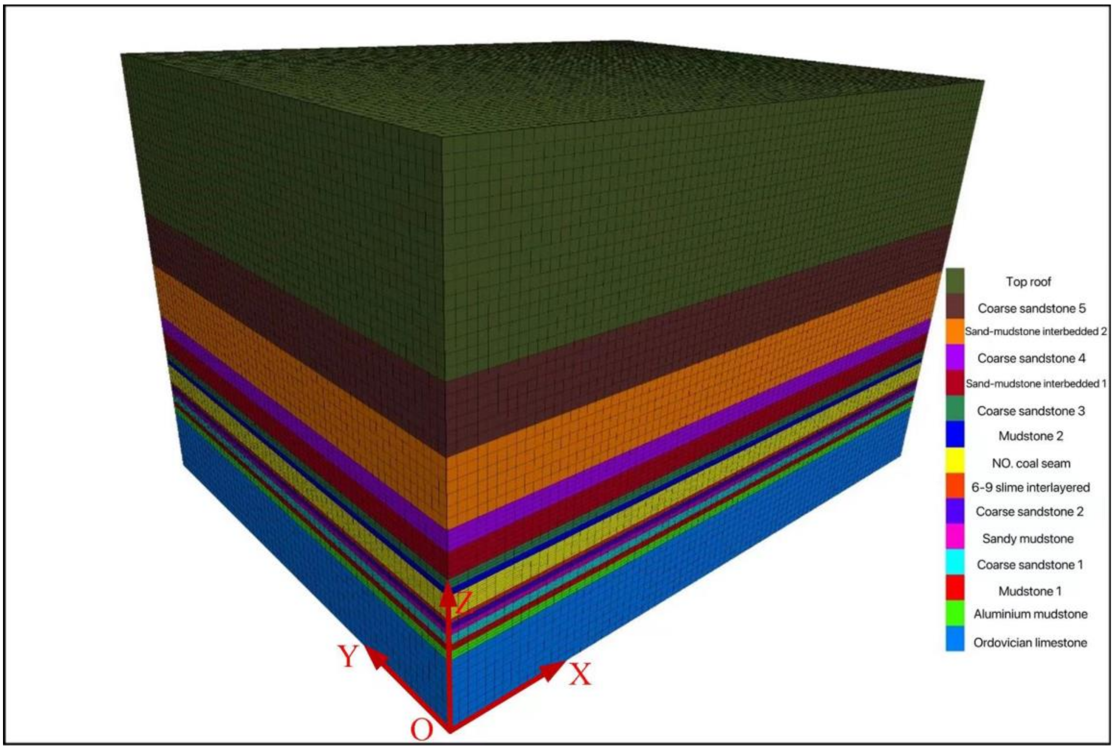

Figure 5. Numerical calculation model.

Based on the current mining conditions, the model's boundary conditions are established: a. Set all stresses and joint velocities to 0. b. Horizontal displacement constraints are imposed on the boundaries in both the X and Y directions of the model, whereas vertical displacement constraints are applied to the bottom boundary. c. When the maximum unbalance force of the model is less than 10^{-5} Pa, it is regarded as the stress equilibrium state, and the excavation can be carried out. The width of the working face measures 250 m, while the maximum advancing distance along the strike is 400 m. To mitigate the boundary effect resulting from the excavation of an extra-thick coal seam, a working face is established with dimensions of 200 m at both the front and rear, and 175 m on each side, as illustrated in Figure 6. The coal seam excavation step is set at 20 m, the calculation time step is 10,000, and the excavation is 20 times in total.

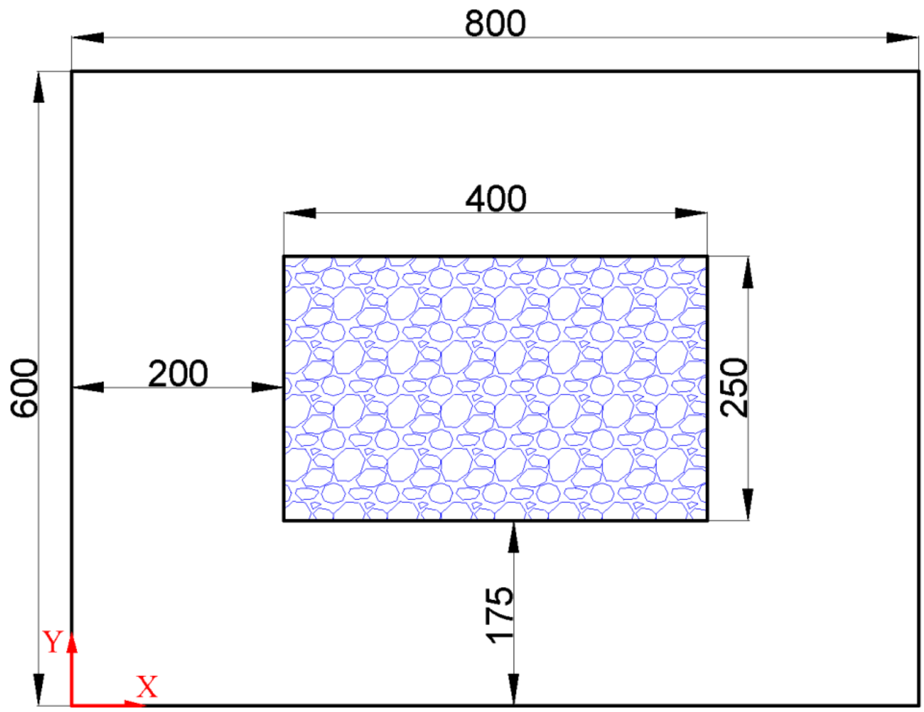

Figure 6. Working surface layout.

3.2.2. Analysis of Model Excavation Results

(1) Characteristics of floor displacement and evolution

Figure 7 illustrates the vertical displacement obtained from the center of the bottom plate at the working face (Y = 300 m, Z = 124.5 m). Figure 8 illustrates the vertical displacement cloud map slices corresponding to various advancing distances during the excavation of the working face. Three directions, X = 0 m, Y = 150 m (working face along the middle), and Z = 124.5 m (coal seam floor), are selected.

a. Due to the excavation of coal seams, the stress in the roof is released, leading to floor heave in the goaf area and resulting in expansion displacement. The maximum floor displacement consistently occurs in the vicinity of the goaf's center.

b. On the vertical section, the displacement contours are "bowl-like" and decrease to the periphery. On the horizontal section, the displacement contours generally form concentric "ellipses". However, the displacement of the coal pillar floor on the advancing side exhibits minor fluctuations due to stress concentration near the coal pillar. Once the decline reaches a certain threshold, the surrounding rock experiences compression as a result of the supporting stress.

c. In the initial phase of mining, the disturbance range caused by rock pressure is limited, resulting in deformation primarily occurring in the surrounding rock adjacent to the goaf. When the working face advances by 40 m, the maximum displacement observed at the floor of the goaf reaches −0.404 m.

d. With the advancement of the working face, the goaf area increases in size, leading to a more significant disturbance effect of ore pressure on the floor. Consequently, the expansion displacement of the floor exhibits both gradual decreases and increases. When mining progresses between 40 and 140 m, the rate of increase is at its peak, rising from 0.404 to 1.05 m. In contrast, during mining operations extending from 140 to 400 m, this increase rate reaches its highest point. The upward expansion displacement of the floor rock mass gradually diminishes and stabilizes over time, with a maximum displacement recorded at approximately −1.26 m.

e. The cantilever beam of the roof, which is formed as a result of mining activities, experiences periodic fracturing and subsequent collapse onto the floor as the working face advances. This results in an uneven stress distribution across the floor within the goaf, leading to a zigzag fluctuation in displacement observed at the center of the goaf.

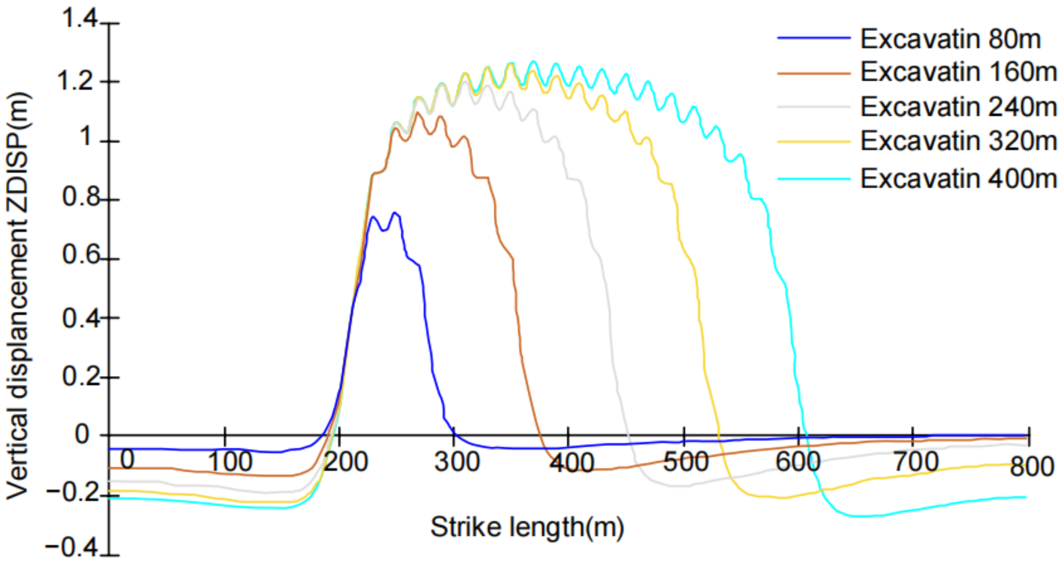

Figure 7. Monitoring the vertical displacement of the middle direction of the working floor.

(2) Evolution characteristics of floor stress

Figure 9 illustrates the vertical stress recorded at the central point of the working face floor (Y = 300 m, Z = 124.5 m). Meanwhile, Figure 10 presents cloud map slices of vertical stress corresponding to various advancing distances during the excavation process of the working face. Three directions of X = 0 m, Y = 150 m (working face along the middle), and Z = 124.5 m (coal seam floor) are selected.

It is evident from the figure that:

a. As the working face advances, the stress within the stope undergoes redistribution. The stress distribution at the top and bottom of the working face exhibits a symmetrical parabolic pattern, with minimum stress occurring directly above and below the working face.

b. A stress concentration zone is observed in the coal pillar located 15–40 m in front of the goaf, with the maximum supporting stress occurring approximately 20 m ahead of the goaf. As mining distance increases, the maximum supporting stress within the coal pillar gradually rises to 18.2 MPa. The support provided by the coal pillar effectively alleviates floor stress, leading to a significant reduction in vertical stress at distances of 5–8 m both in front of and behind the working face. Consequently, expansion displacement begins to manifest within the rock mass of the water-barrier layer, resulting in its degradation.

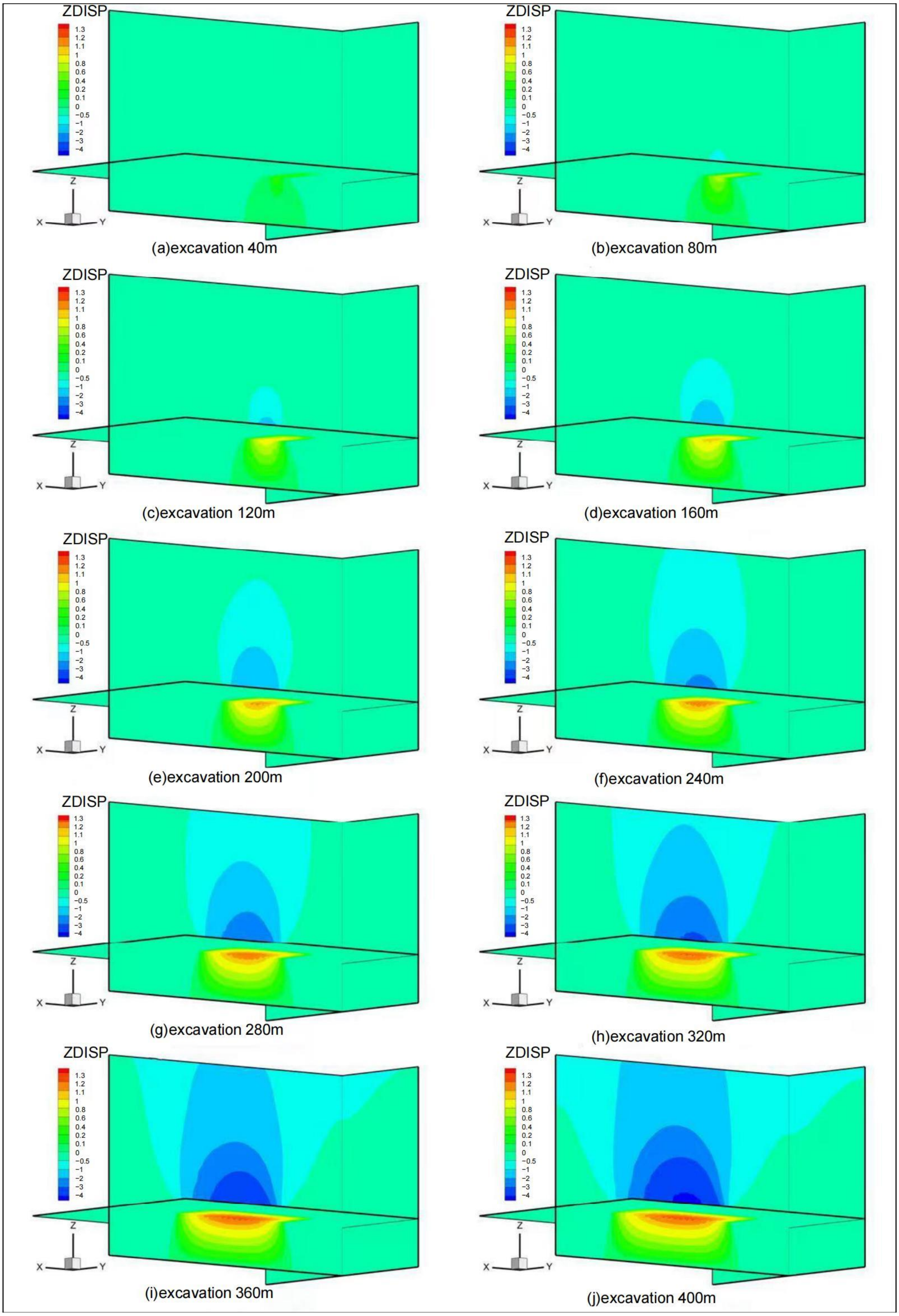

Figure 8. Vertical displacement cloud.

c. In the course of mining, roof failure typically undergoes a process of stratification, bending, fissure, breaking, revolving–caving, etc. As the working face continues to advance, the roof will periodically collapse. As shown in Figure 10, the maximum stress on the measuring line increases from 13.7 MPa when advancing 80 m to 16.1 MPa when advancing 400 m, but the increasing trend is gradually decreasing.

d. When the working face advances to a distance of 40 m, the floor pressure relief zone begins to extend into the Ordovician limestone and subsequently continues to propagate downward. Upon reaching an advance distance of 160 m, the vertical stress variation in the floor approaches a stable state.

e The compressive expansion coefficient of the overlying strata in the goaf has been measured to range from 1.3 to 1.5. Under the mining conditions of a 24.0 m extra-thick coal seam, the roof forms a distinct layer due to the influence of the key stratum, preventing complete re-compaction of the goaf. Additionally, the pressure relief period in the floor after extraction of the extra-thick coal seam is extended, leading to more severe damage to the water barrier within the floor.

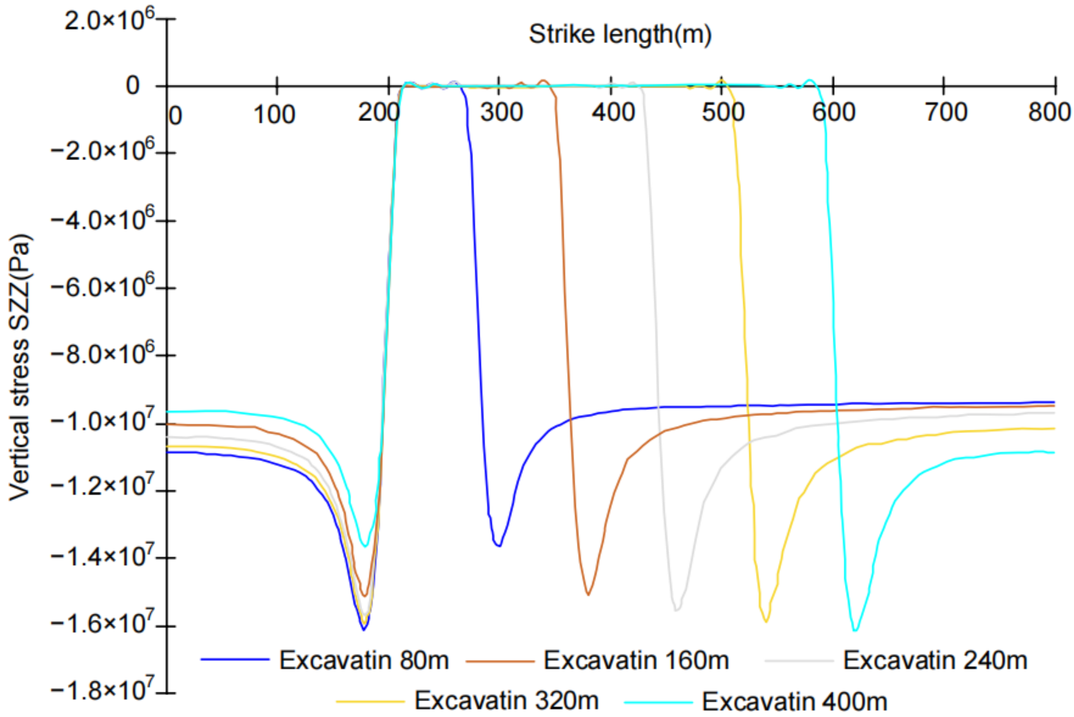

Figure 9. Monitoring of vertical stress in the middle of the working floor.

(3) Analysis of plastic deformation characteristics

The cloud map illustrating the plastic failure characteristics of the coal seam floor at a depth of 300 m is presented in Figure 11:

a. Following the excavation of the working face, the equilibrium of the surrounding stress field is disrupted, leading to a subsequent redistribution of stresses. This phenomenon results in the formation of a stress relief zone within the goaf floor due to stress release, while stress concentration is observed around the periphery of the goaf. Upon advancement of the working face by 20 m, significant plastic deformation becomes evident in the roof and floor of the goaf as well as in the coal pillars on all four sides.

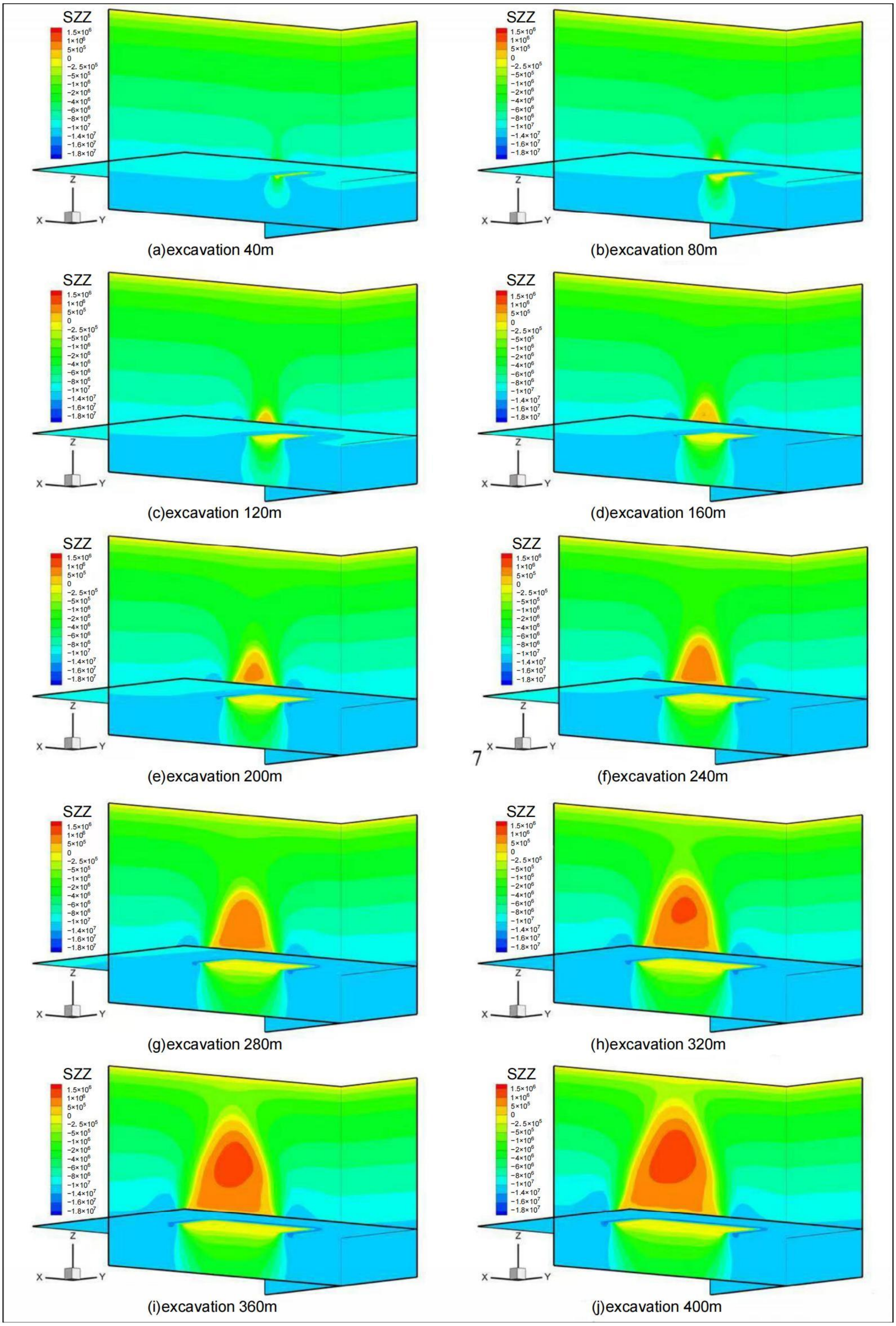

Figure 10. Vertical stress cloud.

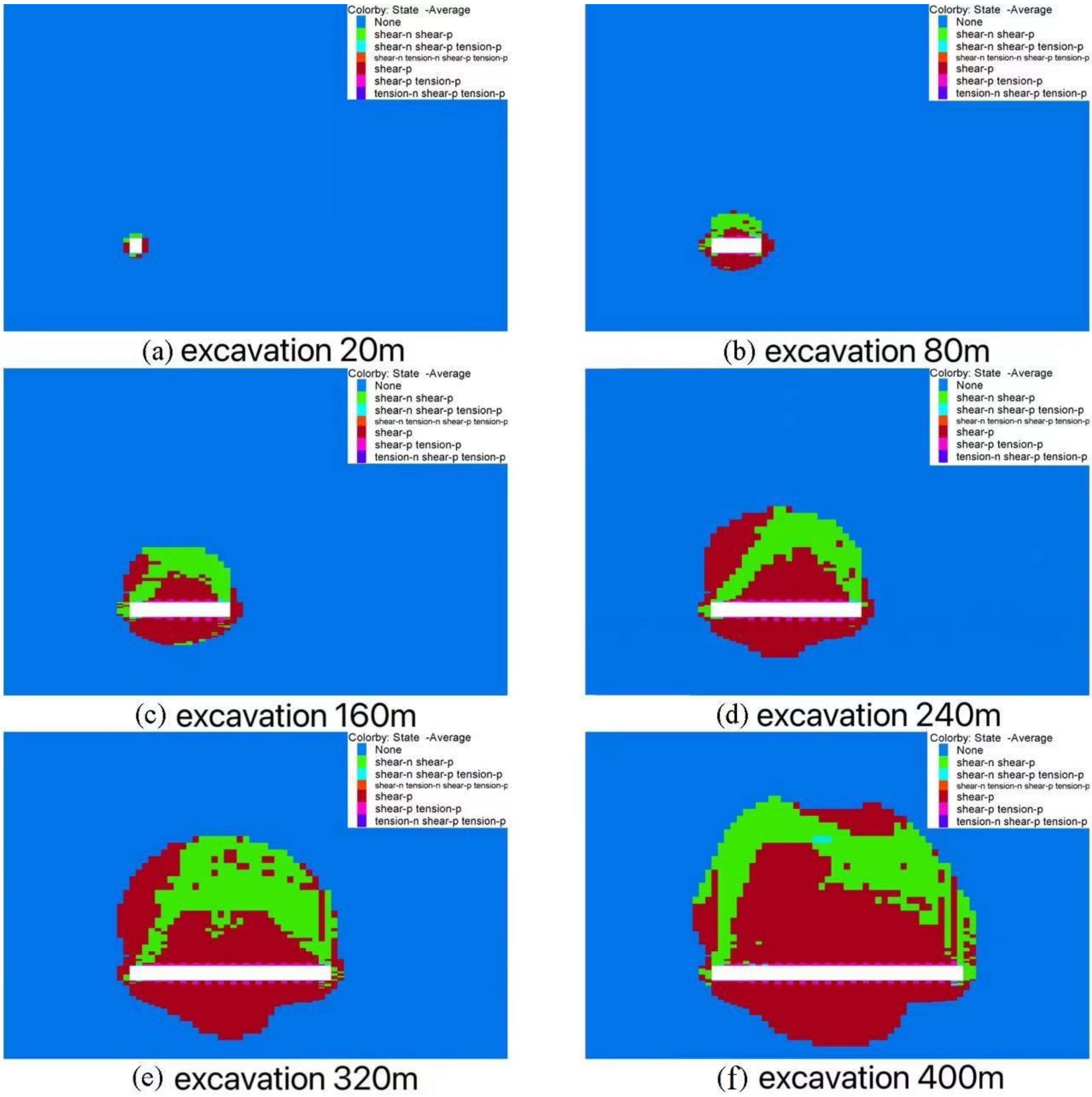

Figure 11. Cloud image of plastic failure of coal seam floor roc.

b. The plastic failure of the floor is predominantly concentrated at and below the immediate bottom of the goaf, with the failure depth increasing as it approaches the center of the goaf. Under a simulation of 10,000 steps, prior to the working face advancing by 160 m, the plastic zone of the floor exhibits a semi-elliptical symmetrical distribution centered on the goaf. However, after the working face has advanced beyond this point, the symmetry of the plastic zone distribution is lost, leading to more pronounced damage on the left side compared to the right.

c. When the working face has been excavated to a depth of 160 m, the plastic zone of the floor extends to the Ordovician limestone interface, resulting in complete plastic failure of the entire water barrier within the floor. The plastic zone extends into the Ordovician limestone layer. However, with the caving of the roof overburden, the goaf is re-loaded, and then the goaf is compressed, and the damage degree of the floor decreases vertically and from top to bottom. The aquifer is not completely permeable to Ordovician limestone water.

4. Evaluation of Floor Water-Inrush Risk by Interval Grey Optimal Clustering Model

This section integrates grey system theory and fuzzy mathematics within the framework of uncertainty mathematics. Utilizing the multi-information integration theory, it focuses on the primary control index system for water inrush as a foundational element. The objective is to classify water-inrush risk by employing an interval grey optimal clustering model to address the uncertainties associated with "small data" and "poor information" that are prevalent in water-inrush risk assessment. The approach aims to thoroughly explore existing information and subsequently predict the risk of floor water-inrush. This prediction will be validated against actual mining hydrogeological conditions, thereby yielding scientifically sound and accurate evaluation results [19].

4.1. Introduction to Interval Grey Optimal Clustering Model

A grey class refers to a collection of observations or objects that belong to the same category. In the primary control index system for floor-water inrush, each main control factor can be categorized into several risk-grade intervals, which are defined as grey classes. Subsequently, utilizing the concept of membership degree, the discrete gray number associated with each main control factor is transformed into an interval gray number through a whitening weight function. This process allows for the fuzzy value of the main control factor to be articulated using precise mathematical language. Following this, based on the comprehensive main control index system, the correlation degree between the evaluation object and its corresponding risk level is computed using grey correlation theory. Finally, by applying optimization theory, an optimal model is established to determine the risk level of the evaluation object [25,26].

4.2. Determination of Whitening Weight Function

The construction of whitening weight function (possibility function) is the prerequisite of an interval grey clustering evaluation model. The function of whiteness weight function clustering is to set the observed objects into different categories in advance. In general, the determination of the whitening weight function should be based on the specific context of the actual problem at hand, not only considering the data distribution characteristics of the observed data itself, but also taking into account the summary of historical experience and knowledge, and determined by a combination of qualitative and quantitative methods to make up for the shortcomings of a single method.

Faced with the complexities and uncertainties associated with water-inrush evaluation, the traditional whitening weight function remains unsolvable. Especially when the significance, dimension, and amplitude of the primary control index factors vary considerably, the influence of certain factors may be disproportionately amplified or diminished. This can result in a distortion of the evaluation outcomes. Therefore, it is necessary to extend the whitening weight function from a single observation value on the real number field to the interval number, and to expand the application range of the whitening weight function.

Definition 1. *There are n cluster objects, m cluster indicators, and p different gray classes, based on the observation value of the $i(i = 1, 2, 3, \ldots, n)$ object on the index $x_{ij}(i = 1, 2, 3, \ldots, n;\ j = 1, 2, 3, \ldots, m)$. The i object is assigned to the $h(h \in \{1, 2, 3, \ldots\ldots, p\})$ gray class, which is named gray clustering.*

Definition 2. *The values of n objects about the indicator j are correspondingly divided into p gray classes, which are called the subclasses of j indicators. The whitening weight function for j indicators within class h is represented as* $f_j^h(\cdot)$.

Definition 3. *Let the owning interval of the h gray standard value corresponding to the j index of the i object be* $\left[y_{jh}(i), y_{j,h+1}(i)\right]$.

Combining the membership function in fuzzy mathematics, we define such a whiteness weight function: each level of the whiteness weight function is not only related to the adjacent upper and lower classes, but also connected to the standard value of each class; this ensures that any measured value of the sample index possesses a non-zero membership degree for every class (with the exception of endpoint values and other specific cases). When $y_{jh} \leq y_{j,h+1}$, the function can be determined by the following formula, and the corresponding whitening weight function can be established in reverse order [27].

$$f_j^h(i) = \begin{cases} 1 & (y_{j1} \leq x_{ij} \leq y_{j2}) \\ \frac{y_{j,p+1}+x_{ij}}{y_{j,p+1}-y_{j1}} & (y_{j2} \leq x_{ij} \leq y_{j,p+1}) \end{cases} \quad (12)$$

$$f_j^h(i) = \begin{cases} \frac{x_{ij}-y_{j1}}{y_{jh}-y_{j1}} & \left(y_{j1} \leq x_{ij} \leq y_{jh}\right) \\ 1 & \left(y_{jh} \leq x_{ij} \leq y_{j,h+1}\right) \\ \frac{y_{j,p+1}-x_{ij}}{y_{j,p+1}-y_{j,h+1}} & \left(y_{j,h+1} \leq x_{ij} \leq y_{j,p+1}\right) \end{cases} \quad (13)$$

$$f_j^h(i) = \begin{cases} \frac{x_{ij}-y_{j1}}{y_{jp}-y_{j1}} & (y_{j1} \leq x_{ij} \leq y_{jp}) \\ 1 & (y_{jp} \leq x_{ij} \leq y_{j,p+1}) \end{cases} \quad (14)$$

(1) Grey correlation analysis

The fundamental concept of grey correlation analysis is to assess the closeness of relationships among different grey correlation factors based on the degree of similarity in the geometric shapes of their corresponding curves. The methodology involves transforming the discrete observed values of each primary control factor into segmented continuous polylines through linear interpolation. Subsequently, a model for determining correlation degrees is constructed based on the geometric characteristics of these polylines. One significant advantage of grey correlation analysis lies in its ability to address issues arising from the absence of typical distributions among primary control factors. Utilizing the whitening weight function established earlier, we redefine the axiom underlying grey correlation thus [28]:

Definition 4. *Let* $F^h(0) = \left(f_1^h(0), f_2^h(0), \ldots, f_m^h(0)\right)$ *as the characteristic behavior of system under the grey class h matrix, and* $F^h(1) = \left(f_1^h(1), f_2^h(1), \ldots, f_m^h(1)\right)$, *……,* $F_j^h(i) = \left(f_1^h(i), f_2^h(i), \ldots, f_m^h(i)\right)$, *……,* $F^h(n) = \left(f_1^h(n), f_2^h(n), \ldots, f_m^h(n)\right)$ *for the related factors under the grey class h sequence,* η_j *for each clustering index weights,* $\sum_{j=1}^{m} \eta_j = 1$, *a given real gamma* $\gamma\left(f_j^h(0), f_j^h(i)\right)$ *content:*

$$\gamma\left(F^h(0), F^h(i)\right) = \sum_{j=1}^{m} \eta_j \gamma\left(f_j^h(0), f_j^h(i)\right) \quad (15)$$

(1) *Standardization:* $0 < \gamma\left(F^h(0), F^h(i)\right) \leq 1$, $\gamma\left(F_j^h(0), F_j^h(i)\right) = 1 \Leftarrow F_j^h(0), F_j^h(i)$;

(2) *Proximity: the smaller* $\left|f_j^h(0) - f_j^h(i)\right|$ *is, the larger* $\gamma\left(f_j^h(0), f_j^h(i)\right)$ *is:*

Then $\gamma\left(F^h(0), F^h(i)\right)$ *is the gray correlation degree of* $F^h(0)$ *and* $F^h(i)$ *in the gray summer of h, and the correlation coefficient of* $\gamma\left(f_j^h(0), f_j^h(i)\right)$ *in the gray summer of* $f_j^h(0)$ *and* $f_j^h(i)$ *about the cluster index of j.*

For correlation coefficient $\gamma\left(f_j^h(0), f_j^h(i)\right)$*, the Dunn grey correlation coefficient formula is adopted, namely:*

$$\gamma\left(x_0^h(j), x_i^h(j)\right) = \frac{\underset{i}{min}\underset{j}{min}\left|f_j^h(0) - f_j^h(i)\right| + \xi\underset{i}{max}\underset{j}{max}\left|f_j^h(0) - f_j^h(i)\right|}{\left|f_j^h(0) - f_j^h(i)\right| + \xi\underset{i}{max}\underset{j}{max}\left|f_j^h(0) - f_j^h(i)\right|} \tag{16}$$

If $F^h(0)$ *has* $f_j^h(0) = 1$ *for any clustering index j, then* $F^h(0)$ *is a clear comprehensive judgment, where* ξ *is the resolution coefficient, generally 0.5.*

(2) Select the optimal model

In order to comprehensively and reasonably describe the proximity between samples i and h gray standard intervals, the proximity degree is expressed by weighted generalized distance with $u^h(i)$ as the weight of the difference degree between samples and each gray standard interval [27]:

$$d^h(i) = u^h(i)\left[\sum_j^m \eta_j f_j^h(i)\right] \tag{17}$$

$u^h(i)$ satisfies $0 \le u^h(i) \le 1$, and $\sum_{k=1}^p u^h(i) = 1$.

Obviously, smaller $d^h(i)$ is always better, so the following multi-factor optimization model is constructed:

$$V - minD = \left(d^1(1), d^2(1), \cdots, d^p(1), \cdots, d^1(n), d^2(n), \cdots, d^p(n)\right) \tag{18}$$

$$s.t.\begin{cases}\sum_{h=1}^p u^h(i) = 1 \quad (i = 1, 2, \cdots, n)\\ 0 \le u^h(i) \le 1\end{cases} \tag{19}$$

The above multi-objective optimization model is transformed into the following equivalent single-objective optimization model:

$$min\left\{F\left(u^h(1)\right)\right\} = min\left\{\sum_{i=1}^n\sum_{h=1}^p\left(d^h(i)\right)^2\right\} = \sum_{i=1}^n\left\{\sum_{h=1}^p\left(u^h(i)\right)^2 \cdot \left[\sum_{j=1}^m \eta_j f_j^h(i)\right]^2\right\} \tag{20}$$

$$s.t.\begin{cases}\sum_{h=1}^p u^h(i) = 1\\ 0 \le u^h(1) \le 1\end{cases} \tag{21}$$

As a Lagrange function:

$$L = \sum_{h=1}^p\left[u^h(i)\right]^2 \cdot \left[\sum_{j=1}^m \eta_j f_j^h(i)\right]^2 - \lambda\left[\sum_{h=1}^p u^h(i) - 1\right] \tag{22}$$

Let $\partial L/\partial u^h(i) = 0$ in parallel to obtain:

$$u^h(i) = \frac{1}{\left[\sum\limits_{j=1}^m \eta_j f_j^h(i)\right]^2} \cdot \sum_{h=1}^p \frac{1}{\left[\sum\limits_{j=1}^m \eta_j f_j^h(i)\right]^2} = \frac{1}{\sum\limits_{k=1}^p\left[\frac{\sum_{j=1}^m \eta_j\gamma\left(f_j^h(0), f_j^h(i)\right)}{\sum_{j=1}^m \eta_j\gamma\left(f_j^k(0), f_j^k(i)\right)}\right]^2} \tag{23}$$

If $\underset{k}{min}u^k(i) = u^{h0}(i)$, Sample i shall be classified as Class h_0.

4.3. Main Control Index System of Extra-Thick Coal Seam Floor Water Inrush

Based on a comprehensive analysis and synthesis of numerous water-inrush incidents in Chinese coal mines over the years, Wu Qiang developed a primary control index system for water inrush occurring in the floor of coal seams during pressured mining [29,30]. The current risk assessment models for floor water inrush, which are based on multivariate information, fundamentally depend on a comprehensive index system specific to floor water inrush. Establishing this comprehensive index system will provide a solid foundation of essential data, critical for the subsequent application of various risk assessment methods related to floor water inrush at the Longwanggou mine.

Based on a systematic analysis of geological data from the Longwanggou Coal Mine and its geological conditions, this work proposes a control index system for floor water inrush that aligns with the water management requirements for the No. 6 coal seam at Longwanggou Coal Mine. This system encompasses 11 critical factors, including water-filled aquifers, geological structures, water-barrier performance, and mine pressure failure (see Figure 12). Among these factors, the presence of water-filled aquifers serves as the foundation for floor water inrush in coal seams; geological structure is identified as a key determinant; mine pressure failure acts as a causative factor; while the prevention measures against water inrush constitute both the condition and context surrounding floor water-inrush events within coal seams.

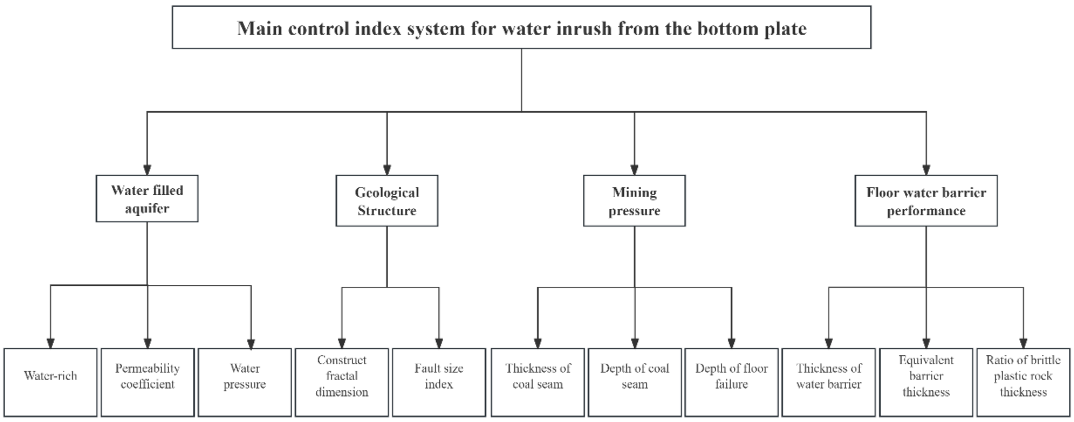

Figure 12. Main control index system for water inrush from NO. 6 coal floor in Longwanggou Coal Mine.

The primary control factors within the system for floor water inrush exhibit spatial characteristics. In this section, we leverage the robust spatial information processing capabilities of Geographic Information Systems software (ArcGIS). Spatial interpolation methods, including Kriging interpolation and inverse distance weighted interpolation, are employed to convert the discrete geological exploration survey data from Longwanggou Coal Mine into continuous data surfaces. This transformation facilitates the representation of these data as three-dimensional spatial information. Then the main control factors can be extracted and analyzed by linear or nonlinear mathematical coupling according to the spatial information [31,32].

4.3.1. Aquifer Containing Water

(1) The Ordovician limestone aquifer serves as the primary aquifer in the pressured mining within the well field. Additionally, it represents a critical focus for preventing water inrush during the extraction process of the coal seam. In this paper, the pumping test data of some boreholes in the well field were collected and ARCGIS was applied to the test holes

by using an inverse distance weighted interpolation method to obtain a thematic map of water-rich areas, as shown in Figure 13a.

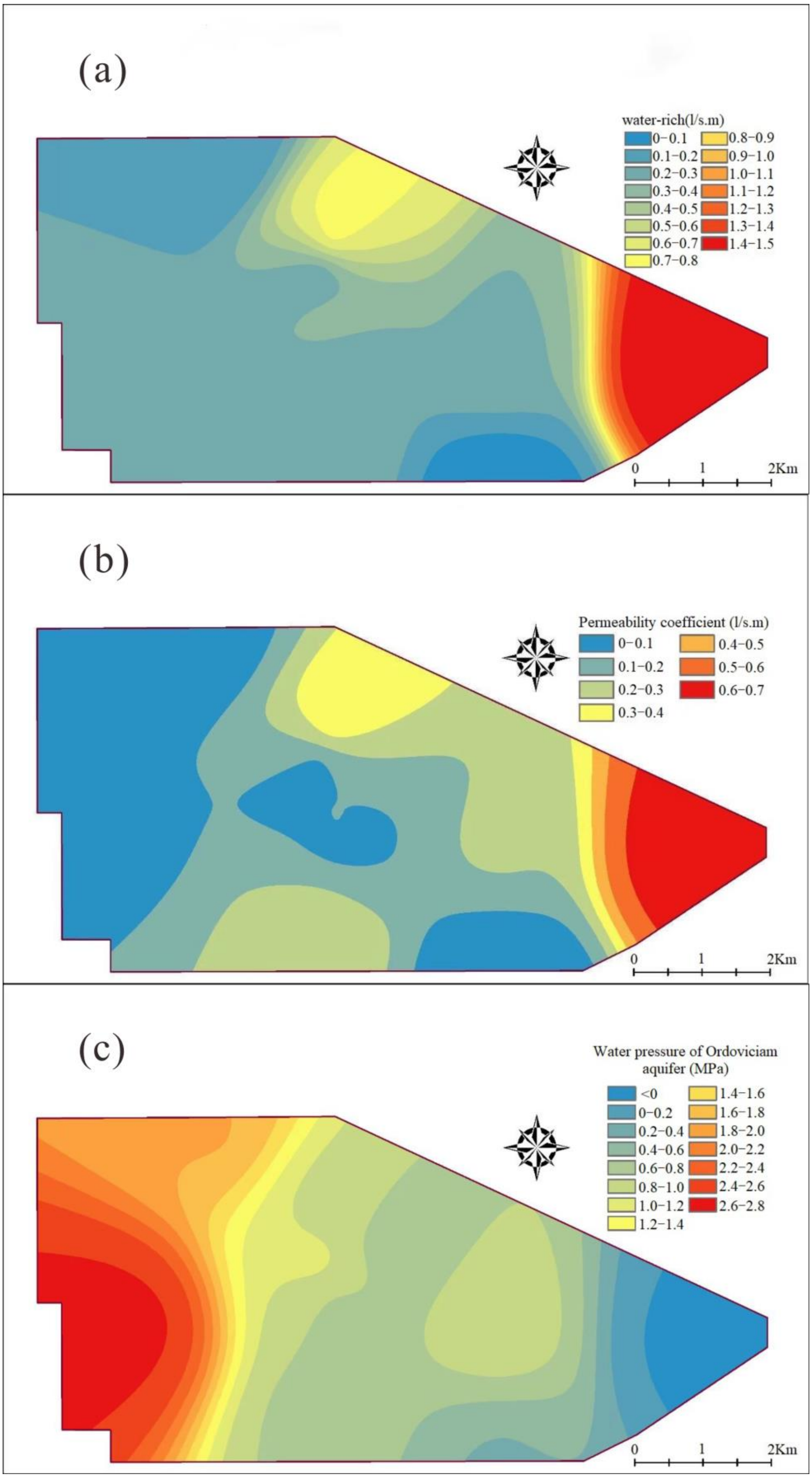

Figure 13. Water filled aquifer. (**a**) Water-rich. (**b**) Permeability coefficient. (**c**) Water pressure of Ordovician aquifer.

(2) The permeability coefficient functions as the principal index for quantifying the water permeability characteristics of aquifer rock strata. This coefficient is directly correlated with the degree of permeability within these strata. A higher permeability coefficient signifies more frequent dynamic interactions between aquifers, thereby enhancing the water richness of the aquifer system. Based on partial permeability coefficient data from the Longwanggou mining area, an interpolated thematic map depicting the permeability coefficient of Ordovician limestone aquifers in the Longwanggou Coal Mine, as shown in Figure 13b, has been constructed.

(3) Aquifer water pressure acts as the principal driving force for floor water-inrush events. The essential mechanism of floor water inrush is that when the hydraulic head pressure surpasses the confining strength of the aquiclude, the likelihood of such incidents significantly increases. The main recharge source of Ordovician limestone groundwater in Longwanggou Mine is the Yellow River water, followed by the atmospheric precipitation recharge, which shows the dynamic characteristics of meteorological type. According to the hydrologic pore data, a special water pressure map of Ordovician ash in Longwanggou Coal Mine was obtained, Figure 13c.

4.3.2. Geological Structure

(1) In order to quantitatively evaluate the structural complexity from the plane, fractal theory is used to study the overall structural complexity of faults, folds, and abnormal areas in the mine field, and fractal dimension is used to quantify the complexity of regional fault structures. The greater the fractal dimension, the more advanced the structures become; conversely, a smaller fractal dimension indicates less developed structures. The thematic map of structural complexity in Figure 14a is obtained by using GIS and Kriging interpolation.

(2) The scale of faults includes fault length, cutting depth, number, and quantity of fault groups. The greater the length of the fault, the deeper the incision, and the more numerous the development groups, along with an increased scale advantage, which all contribute to a heightened influence on water inrush from the coal seam floor. The concept of the “fault scale index” presented here pertains to the magnitude of fault systems and is defined as the cumulative product of the extension length and vertical displacement of all faults within a unit area. The fault scale index exhibits a positive correlation with the risk of water inrush [33,34]. All the faults in the Longwanggou Coal Mine field are tensile normal faults which can easily become water channels. The thematic map of fault size index in Figure 14b was obtained by using GIS Kriegin interpolation.

4.3.3. Performance of Waterproof Layer

(1) This study quantifies the thickness of the water barrier between the floor and Ordovician limestone using data from 12 hydrological boreholes. Furthermore, Geographic Information System (GIS) technology was employed to generate Figure 15a, a thematic map that visually represents the distribution and thickness of the water barrier.

(2) The water retention capacity of the water-retaining layer is influenced by its thickness, mechanical strength, and lithological sequence. Consequently, the rock strength equivalence coefficient is utilized to convert the thicknesses of both the water-retaining layer and the rock layers with varying lithologies into their respective equivalent thicknesses [35]. Subsequently, the equivalent thickness of the water-retaining layer is aggregated to produce the specialized map illustrating equivalent water-retaining layer thickness, as shown in Figure 15b.

(3) Variations in the lithology and proportion of water-retaining rock sections in coal seam floors result in significant differences in mechanical strength, as well as markedly different water-blocking performance and stability. Under identical conditions, brittle sand-

stone layers or carbonate rock layers exhibit higher mechanical strength and superior surge prevention performance. Conversely, mud shale rocks or coal layers, which exhibit plastic behavior, possess lower mechanical strength and demonstrate inferior surge prevention capabilities [29]. Therefore, a higher thickness ratio of brittle-plastic rock correlates with enhanced water barrier performance, as illustrated in Figure 15c.

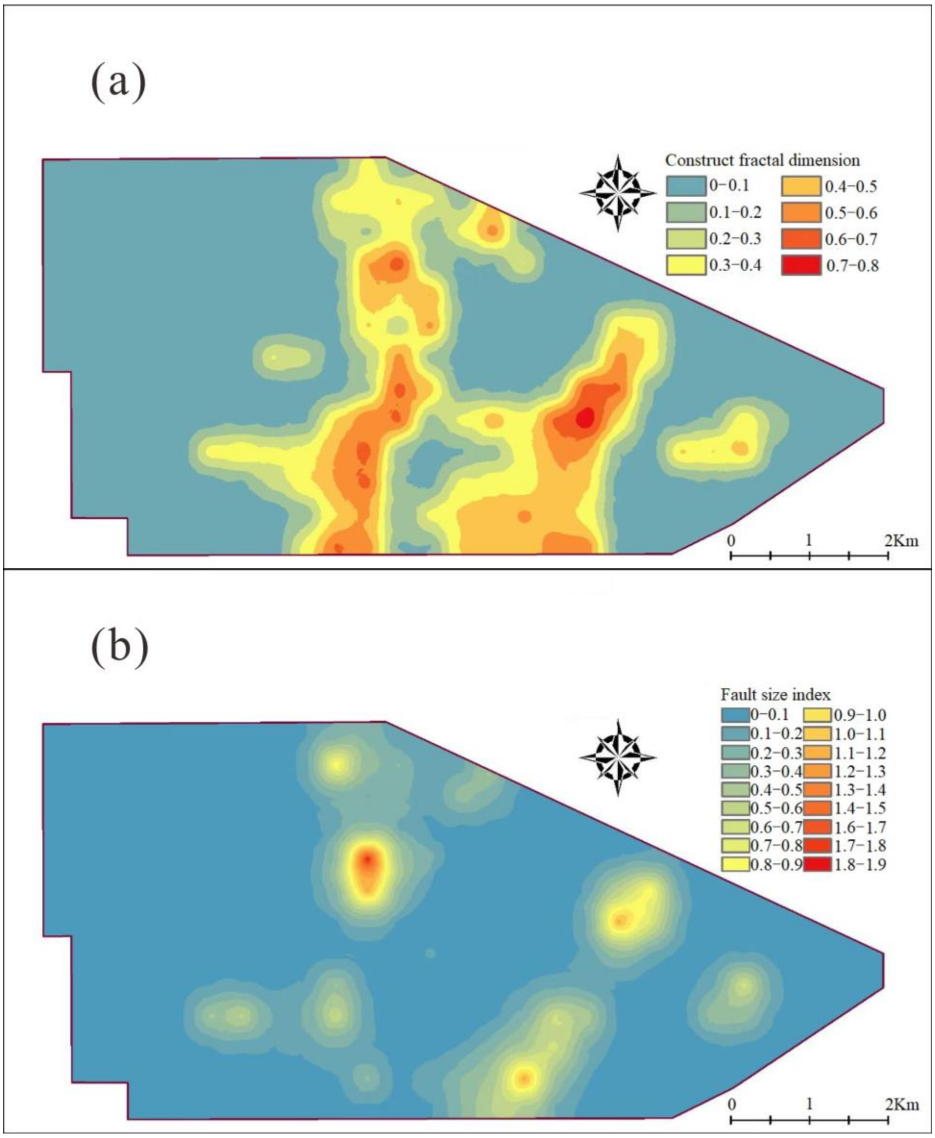

Figure 14. Geological structure. (**a**) Construct fractal dimension. (**b**) Fault size index.

4.3.4. Mine Pressure Failure

(1) As the mining height increases, the vertical stress on the floor decreases, leading to an increase in the vertical displacement of the surrounding rock. Consequently, the gradient of the displacement isoline diminishes, while the failure depth of the floor escalates [8]. The reserve information of the No. 6 coal seam has been calculated based on data from 157 boreholes within the well field. The thickness of the No. 6 coal seam at Longwanggou Mine, as illustrated in Figure 16a, is derived through Kriging interpolation.

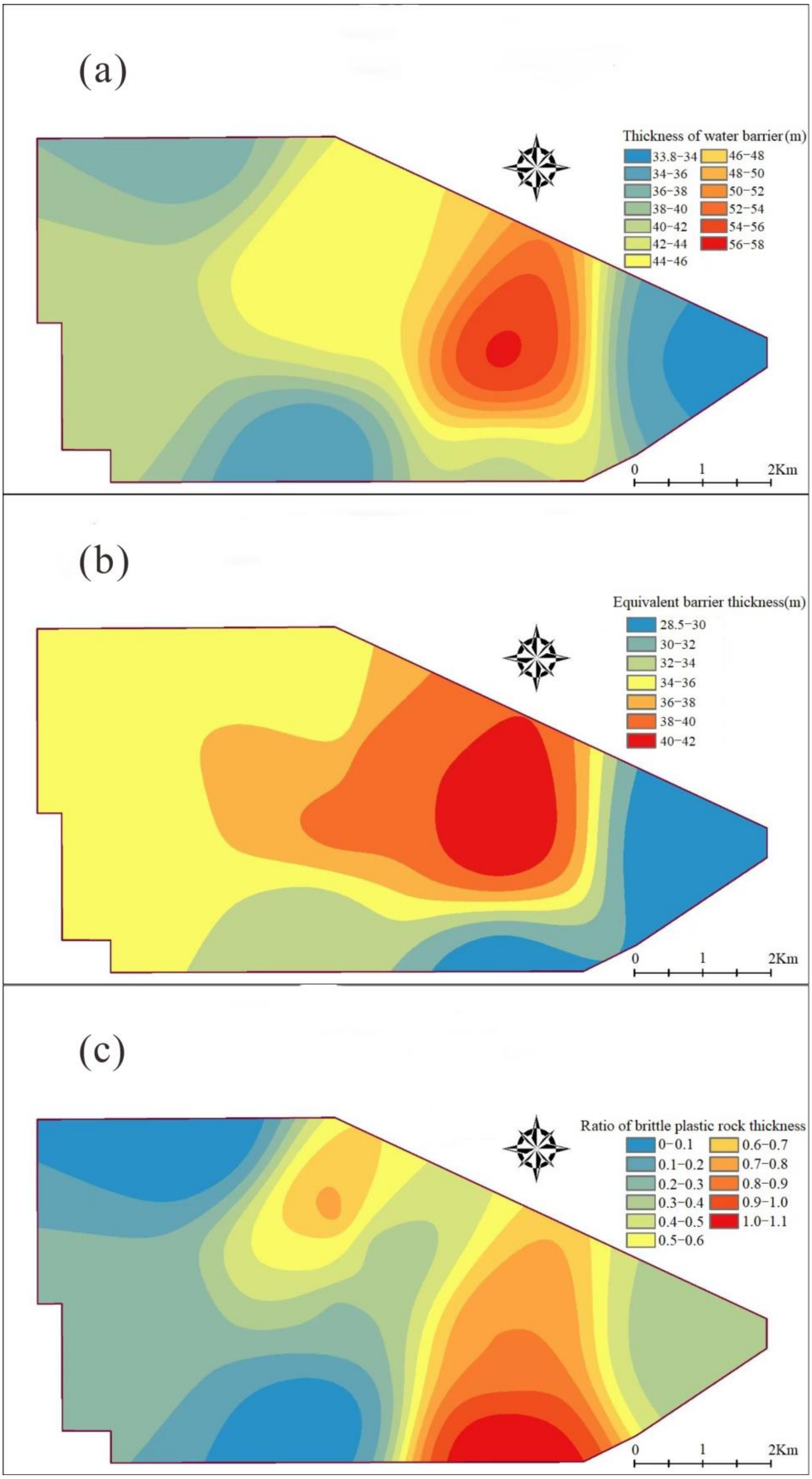

Figure 15. Floor water barrier performance. (**a**) Thickness of water barrier. (**b**) Equivalent barrier thickness. (**c**) Ratio of brittle plastic rock thickness.

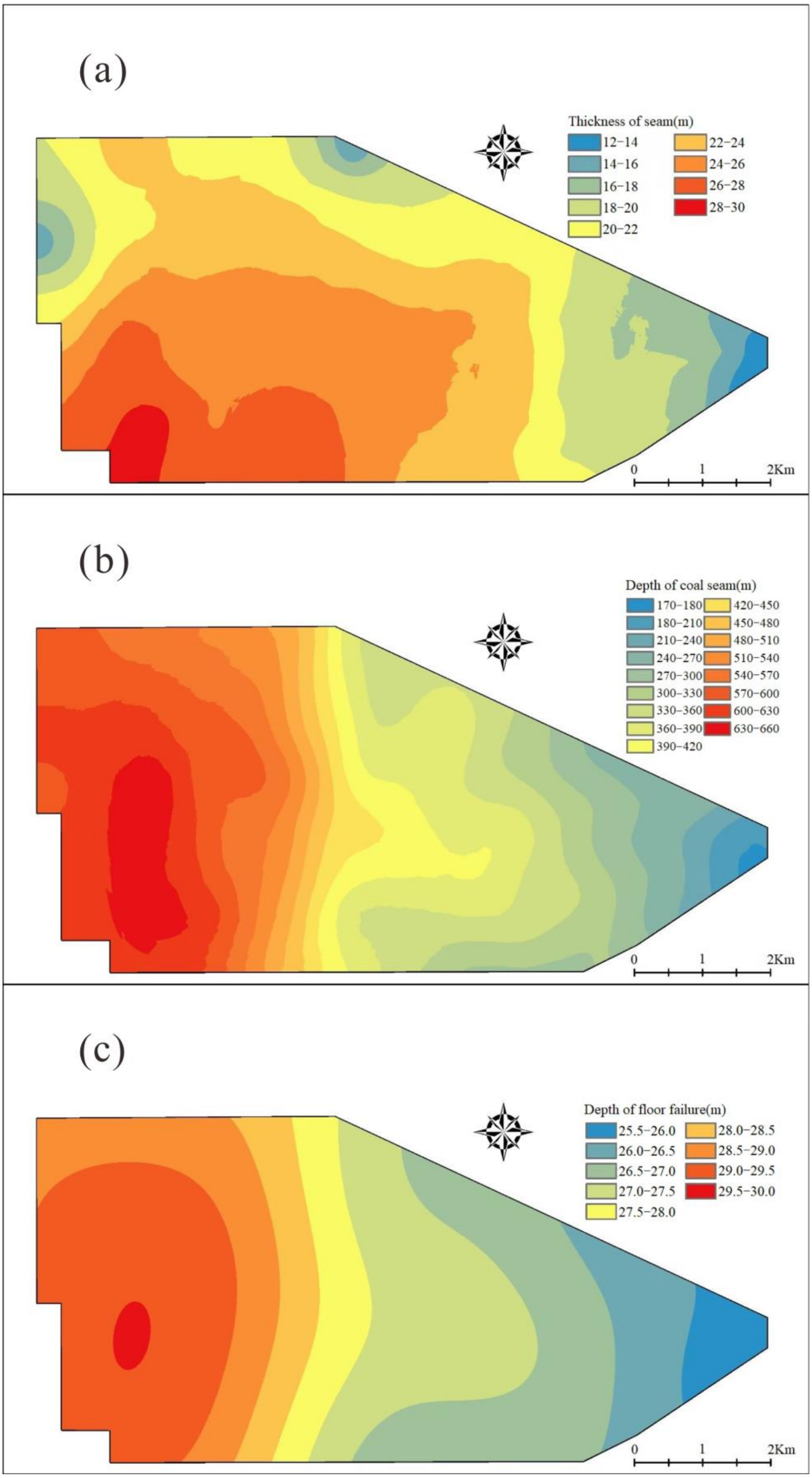

Figure 16. Mine pressure mining conditions. (**a**) Thickness of coal seam. (**b**) Depth of coal seam. (**c**) Depth of floor failure.

(2) The mining depth of coal seams significantly influences the original stress state of the surrounding rock strata. As the mining depth increases, the original stress within these coal rock strata also escalates. Consequently, following the extraction at the working face, the pressure-relief zone in the floor expands, leading to a more pronounced deterioration of the waterproof layer in that area. According to the information of coal seam buried depth of 157 boreholes in the well field, the special topic of Longwanggou No. 6 coal seam buried depth in Figure 16b is obtained by Kriging interpolation.

(3) The empirical and theoretical formulas (China's coal industry) for calculating the failure depth of the floor are adopted [36]:

$$h = 0.0085H + 0.1665\alpha + 0.1079L - 4.3579 \tag{24}$$

h—Floor failure depth (m):

L—Working face length (m):

H—Depth of coal seam (m):

α—Coal seam inclination (°).

According to the data from the 61,601 working faces in study area, L is 255 m and α is 4°. Formula (24) is substituted into Figure 16b, and the failure depth Figure 16c is obtained by ArcGIS grid calculation.

4.4. Weight and Interval Division of Main Control Factors

4.4.1. Interval Division of Main Control Factors

Cluster analysis is a data reduction technique aimed at categorizing data objects into multiple classes or clusters based on specific criteria. Each class or cluster has a high similarity, and there is a large difference between different classes or clusters. Cluster analysis can mine valuable information from the vast and disordered data [37,38].

In this paper, the K-Means clustering algorithm is employed to partition the intervals of primary control factors. This algorithm falls under the category of unsupervised learning and does not require a predefined training set. It is characterized by its straightforward principle, ease of implementation, rapid convergence, and clear interpretability of results. The following section provides a brief overview of the algorithm's concept [39]: a. Determine the number of clusters K, and randomly select K data points as the initial cluster centroids. b. Calculate the distance between each data point and every cluster centroid, and assign each data point to the cluster with the nearest centroid. c. Compute the mean of the data points within each cluster to obtain the new cluster centroids. d. Repeat steps b to c until the cluster centroids stabilize or the maximum number of iterations is reached.

According to the actual situation of Longwanggou Coal Mine, the thematic maps of 11 main control factors were covered by a grid with the same spatial position (400 m × 400 m) and divided into 284 grids. The average values of each primary control factor within the grid were calculated for each partition, and the average values of the grid were represented by the coordinate positions at the center of the grid.

The classification based solely on the unsupervised self-learning of the K-means clustering algorithm cannot reflect the nonlinear dynamic characteristics of each main control factor. The methodology employed in this paper involves initially setting the value of K to 10. Subsequently, leveraging the knowledge and expertise of industry professionals, we systematically categorized it into four distinct level intervals. These intervals are designated based on the severity of impact associated with water-inrush incidents: the intervals of the main control factors of safety, safety, danger, and danger are shown in Table 2 below.

Table 2. Dangerous level division and weight coefficient of main controlling factors of floor water inrush.

Main Control Factor / Weight and Rank	Safe		Safer		More Dangerous		Dangerous		Weight Coefficient
Water-rich (L/s·m)	0	0.19	0.19	0.48	0.48	1.00	1.00	1.50	0.0654
Permeability coefficient (m/d)	0	0.10	0.10	0.20	0.20	0.40	0.40	0.64	0.036
Water pressure (MPa)	−0.10	0.20	0.20	1.10	1.10	2.10	2.10	2.65	0.1189
Construct fractal dimension	0	0.12	0.12	0.25	0.25	0.44	0.44	0.70	0.06
Fault size index	0	0.13	0.13	0.36	0.36	0.84	0.84	1.17	0.03
Thickness of coal seam (m)	12.60	17.60	17.60	22.20	22.20	25.90	25.90	28.40	0.1861
Depth of coal seam (m)	176.00	310.00	310.00	407.00	407.00	552.00	552.00	644.00	0.1024
Depth of floor failure (m)	25.50	26.50	26.50	27.40	27.40	28.40	28.40	29.60	0.0564
Thickness of water barrier (m)	56.10	51.20	51.20	44.50	44.50	37.20	37.20	33.50	0.0583
Equivalent barrier thickness (m)	41.30	38.00	38.00	34.10	34.10	30.20	30.20	28.50	0.1336
Ratio of brittle plastic rock thickness (%)	1.07	0.82	0.82	0.49	0.49	0.29	0.29	0	0.1529

4.4.2. Utilizing the Analytic Hierarchy Process to Establish Weight Coefficients

AHP is utilized rto decompose complex problems into multiple component factors, and to further decompose these factors according to the domination relationship, and arrange them according to the target layer, criterion layer, and index layer, forming a multi-objective and multi-level model and forming an orderly hierarchical structure [40]. According to Figure 12, a hierarchical analysis structure model has been established, categorizing the research subjects into three levels. In this model, the risk assessment of water inrush from the Longwanggou Coal Mine is designated as target layer A. The performance of the water-filled aquifer, geological structure, mining pressure, and water-barrier layer constitutes criterion layer B. Additionally, eleven primary control factors form decision level C, as illustrated in Figure 17.

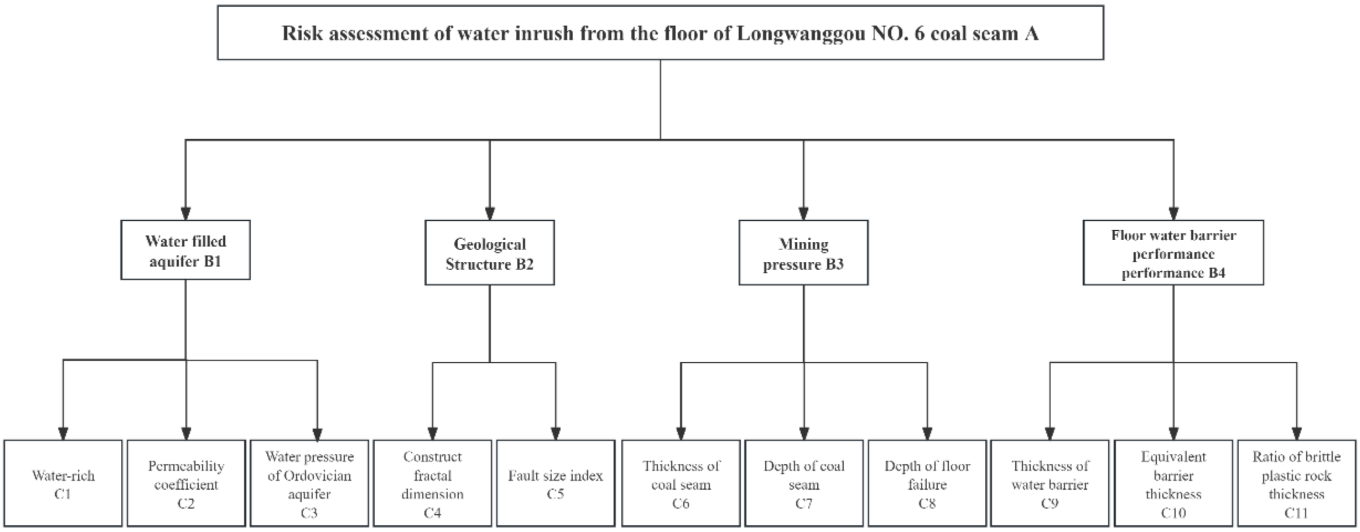

Figure 17. Analytic hierarchy process structural model for risk assessment of water inrush from coal floor.

The issue addressed by AHP involves determining the relative weights of elements in the lowest layer with respect to those in the highest layer, as shown in Table 3. The hierarchical judgment matrix is formulated through a pairwise comparison method, which assesses the relative importance of all factors within a given layer in relation to a specific criterion from the upper layer.

Table 3. Element matrix of judgment matrix.

Scale	Implication
1	Indicates that two factors are equally important when compared
3	Indicates that one factor is slightly more important than the other when comparing two factors
5	Indicates that one factor is significantly more important than the other
7	Indicates that one factor is strongly more important than the other when comparing two factors
9	Indicates that one factor is extremely important compared to the other
2, 4, 6, 8	The median of the two adjacent judgments above
Count backwards	The judgment of comparing factor i with j, then the judgment of comparing factor j with i: $a_{ji} = 1/a_{ij}$

Experts who are familiar with the hydrogeology of Junge Coal Field or Longwanggou Coal Mine are invited to score according to the scale in Tables 4–8, establish the hierarchical judgment matrix, and conduct a consistency test, as shown in Tables 4–8. The weight of each controlling factor obtained in the end is reshown in Table 2.

Table 4. Judgment matrix $A\sim B_i(i = 1\sim 4)$.

A	B_1	B_2	B_3	B_4	$W(A/B)$
B_1	1	4	1/2	1/2	0.2203
B_2	1/4	1	1/3	1/3	0.09
B_3	2	3	1	1	0.3449
B_4	2	3	1/1	1	0.3449

Table 5. Judgment matrix $B_1\sim C_i(i = 1\sim 3)$.

B_1	C_1	C_2	C_3	W
C_1	1	2	1/2	0.297
C_2	1/2	1	1/3	0.1634
C_3	2	3	1	0.5396
$\lambda max = 3.0092,\ CR = 0.00885,\ CI = 0.00460136 \leq 0.1$				

Table 6. Judgment matrix $B_2\sim C_i(i = 4\sim 5)$.

B_2	C_4	C_5	W
C_4	1	2	0.6667
C_5	1/2	1	0.3333
$\lambda max = 2,\ CR = 0,\ CI = 0 \leq 0.1$			

Table 7. Judgment matrix $B_3\sim C_i(i = 6\sim 8)$.

B_3	C_6	C_7	C_8	W
C_6	1	2	3	0.5396
C_7	1/2	1	2	0.297
C_8	1/3	1/2	1	0.1634
$\lambda max = 3.0092, CR = 0.00885,\ CI = 0.00460136 \leq 0.1$				

Table 8. Judgment matrix $B_4 \sim C_i (i = 9 \sim 11)$.

B_4	C_9	C_{10}	C_{11}	W
C_9	1	1/2	1/3	0.1692
C_{10}	2	1	1	0.3874
C_{11}	3	1/1	1	0.4434

4.5. Evaluation Results of Interval Grey Optimal Clustering Model

The values of each primary control factor in the grid are put into the corresponding whitening weight function, and the membership degree relationship between them and each risk level is obtained. Then, the correlation degree matrix between the sampling points and each risk level is calculated by using Deng's grey correlation theory. Then the correlation degree matrix is brought into the optimal model for calculation, and the risk result is obtained. Finally, the GIS delineates the water inrush risk assessment zones for the floor of coal seam at Longwanggou Mine, as illustrated in Figure 18.

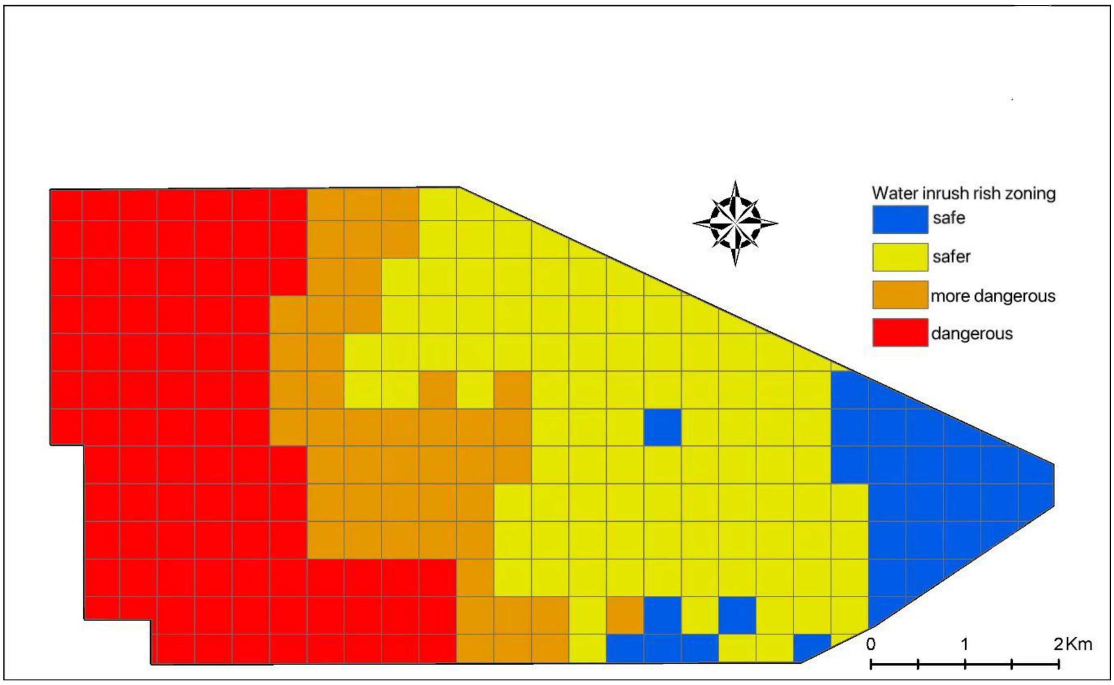

Figure 18. Zoning map for risk assessment of water inrush from Longwanggou NO. 6 coal seam floor.

According to Figure 18, the areas of safe, safer, more dangerous, and dangerous areas accounted for 10.79%, 37.91%, 18.10%, and 33.19%, respectively. Based on the evaluation results of water-inrush risk, this study proposes a comprehensive approach to floor water prevention and control. The strategy emphasizes "zoning evaluation to identify hidden dangers; precise exploration with probing preceding excavation; grouting transformation ensuring treatment precedes mining; and full-process monitoring for comprehensive defense." This integrated methodology prioritizes proactive regional management of Austrian ash layers to ensure safe mining operations. Furthermore, the grid analysis based on the risk assessment of water inrush from the floor of the No. 6 coal seam at Longwanggou Mine reveals a zonal clustering effect. The areas identified as hazardous are predominantly located in the western section of the mining field. The risk of floor water inrush decreases from west to east. The result of risk assessment is composed of 11 main control factors; no one factor has absolute advantage, and the information of each factor is fully used. In addition, the weights and rank interval values obtained through expert knowledge and experience enhance the pertinence of the data.

5. Discussion

In this paper, the assessment of water inrush from the coal seam floor integrates multiple disciplines, including hydrogeology, engineering geology, rock and soil mechanics, GIS, and grey system theory. Due to limitations in the authors' expertise and available data, several areas require further improvement: (1) The analysis of the failure mechanism of the floor should incorporate in situ stress and strain measurements alongside rock and soil mechanics theory and computer numerical simulations. (2) Laboratory-derived physical and mechanical parameters of rock and soil masses are often influenced by structural features such as joints and cracks, leading to discrepancies with actual field conditions. Applying an appropriate reduction or amplification factor can enhance the accuracy of FLAC3D numerical simulation results. (3) The precision of geographic information significantly impacts the assessment of water-inrush risk on the floor. To improve accuracy, the evaluation methodology should align with advancements in 3D geological transparency, enhancing key control factors through improvements in spatial precision, temporal accuracy, and attribute fidelity. This can be achieved by leveraging advanced technologies such as big data analytics, artificial intelligence, the Internet of Things, and cloud computing, ensuring reliable predictive outcomes. Future assessments of water-inrush risk should enable real-time dynamic monitoring and adaptation.

6. Conclusions

(1) Under the mining conditions of extra-thick coal seams, the floor can be categorized into three distinct zones: the floor failure zone, the transition zone (characterized by plastic deformation failure), and the weathering zone at the Ordovician limestone top interface. Based on theoretical analyses derived from soil mechanics and mine pressure considerations, it is established that there exists a linear relationship between coal seam thickness and floor failure depth; specifically, as the thickness of the coal seam increases, so does the depth of floor failure.

(2) The numerical simulation results show that with the excavation of the working face, floor heave occurs at the center of the goaf's floor, leading to expansion displacement. Consequently, the displacement of the floor diminishes from top to bottom. The maximum displacement of the floor stabilizes after reaching approximately 1.26 m. The stress distribution at both the top and bottom of the working face exhibits a symmetrical parabolic pattern, with the maximum stress on the coal pillar—both before and after the goaf—increasing in correlation with the advancing distance. When the working face is advanced to 40 m, the pressure relief zone beneath the bottom plate begins to extend into the Ordovician limestone and subsequently continues to expand downward. Upon reaching 160 m, the vertical variation in bottom stress stabilizes. The pressure relief time of the bottom plate is extended, resulting in more severe damage to the bottom plate. As excavation progresses at the working face, the development of the plastic zone becomes distinctly evident in both the vertical direction at the top and bottom of the goaf. Before the excavation of the working face at a depth of 160 m, the plastic zone on the bottom floor exhibits a semi-elliptical symmetrical distribution along the center of the goaf. However, as excavation progresses, this symmetry in the distribution of the plastic zone begins to diminish, resulting in more severe damage on the left side compared to that on the right side. When the excavation at the working face reaches 160 m, the plastic zone at the bottom floor extends to the interface of the Ordovician limestone. However, as the overlying rock roof collapses, the goaf experiences reloading. Subsequently, part of the goaf becomes

compacted, resulting in a vertical decrease in damage severity from top to bottom within the floor.

(3) Based on the theory of multi-information integration, we propose a novel method known as the interval grey optimal clustering model. This approach is specifically designed for assessing water-inrush risk in the floor of Longwanggou Coal Mine. It synthesizes two primary research methodologies addressing uncertainty: grey series theory and fuzzy mathematics. Based on the geographic information obtained from the main control index system for coal seam floor water inrush, and leveraging the robust spatial information processing capabilities of GIS as technical support, the entire mine has been categorized into four levels: safe, relatively safe, more dangerous, and dangerous. The regional distribution and area size information for each risk level have been derived through model calculations. The safe, moderately safe, somewhat dangerous, and dangerous areas are 10.79%, 37.91%, 18.10%, and 33.19%, respectively. The results indicate that the grid generated from the assessment of water-inrush risk associated with the No. 6 coal seam at Longwanggou Mine exhibits a zonal clustering effect. Dangerous areas are predominantly located in the western part of the mining field, while the risk of water inrush from the floor diminishes progressively from west to east. The proposed methodology has significantly enhanced the theoretical framework for assessing floor water-inrush risks, providing a crucial foundation for the safe extraction and sustainable development of analogous mining operations.

Author Contributions: Writing—original draft, M.C. and S.Y.; Investigation, H.L.; Software, X.W. and W.X.; Methodology, G.W. and S.L.; Data curation, Q.L. All authors have read and agreed to the published version of the manuscript.

Funding: This research were funded by Ministry of Science and Technology of China, grant number 2024YFC3013802 and Langfang Science and Technology Bureau, grant numbers 2024013022, 2024011064.

Data Availability Statement: The data supporting the findings of this study are openly available on https://www.cnki.net (accessed on 2 February 2025).

Conflicts of Interest: Qixing Li is employed by National Energy Yili Energy Co., Ltd. The authors declare no potential conflicts of interest with respect to the research, authorship, and/or publication of this article.

References

1. Cao, M.; Yin, S.; Xu, B. Water inrush and failure characteristics of coal seam floor over a confined aquifer. *Energy Rep.* **2021**, *7*, 8298–8311. [CrossRef]
2. Shuai, Z.; Shuqian, L.; Shangxian, Y.; Manyu, L.; Haopeng, M.; Rongrong, Q.; Yuanyuan, L. A new type of Ordovician limestone karst water inrush from the floor of old goaf: Formation mechanism and the prevention and control technology. *Coal Geol. Explor.* **2023**, *51*, 12.
3. Esterhuizen, G.; Bajpayee, T.; Murphy, M.; Ellenberger, J. Evaluation of the strength reduction method for US coal mine entry stability analysis. In *Ground Support 2013: Proceedings of the Seventh International Symposium on Ground Support in Mining and Underground Construction*; Australian Centre for Geomechanics: Crawley, WA, Australia, 2013. [CrossRef]
4. Howlader, M.; Deb, P.; Shahidul Haqe Mazumder, A.T.M.; Ahmed, M. Evaluation of water resources around Barapukuria coal mine industrial area, Dinajpur, Bangladesh. *Appl. Water Sci.* **2014**, *4*, 203–222. [CrossRef]
5. Zhu, S.; Jiang, Z.; Zhou, K.; Peng, G.; Yang, C. The characteristics of deformation and failure of coal seam floor due to mining in Xinmi coal field in China. *Bull. Eng. Geol. Environ.* **2014**, *73*, 1151–1163. [CrossRef]
6. Zhang, P.; Liu, C.; Ou, Y.; Sun, B.; Xu, S.; Li, S. Comprehensive testing research on floor damage characteristics of mining extra-thick seam in Jungar Coalfield. *Coal Geol. Explor.* **2021**, *49*, 30.
7. Fu, B.; Tu, M.; Cheng, Y. Deformation and failure characteristics research on thick seam mining floor above confined water. *Chin. J. Undergr. Space Eng.* **2017**, *13*, 107–112.
8. Xu, Y.Y. Applicability analysis on statistical formula for failure depth of coal seam floor in deep mine. *Coal Sci. Technol.* **2013**, *41*, 129–132. [CrossRef]

9. Cao, M.; Yin, S.; Li, S.; Wang, X. Mechanisms of Thick-Hard Roof and Thin Aquifer Zone Floor Destruction and the Evolution Law of Water Inrush. *Water* **2024**, *16*, 2304. [CrossRef]
10. Zhang, R.; Jiang, Z.; Yue, Z.; Zhao, L.; Yu, X. In-situ dynamic observation and numerical analysis of thick coal seam floor's failure law under the mining. *J. Min. Saf. Eng.* **2012**, *29*, 625.
11. Sun, X.; Zhao, C.; Zhang, Y.; Chen, F.; Zhang, S.; Zhang, K. Physical model test and numerical simulation on the failure mechanism of the roadway in layered soft rocks. *Int. J. Min. Sci. Technol.* **2021**, *31*, 291–302. [CrossRef]
12. Li, A.; Mu, Q.; Ma, L.; Liu, C.; Wang, S.; Wang, F.; Mou, L. Numerical Analysis of the Water-blocking Performance of a Floor with a Composite Structure under Fluid–solid Coupling. *Mine Water Environ.* **2021**, *40*, 479–496. [CrossRef]
13. Mo, S.; Sheffield, P.; Corbett, P.; Ramandi, H.L.; Oh, J.; Canbulat, I.; Saydam, S. A numerical investigation into floor buckling mechanisms in underground coal mine roadways. *Tunn. Undergr. Space Technol.* **2020**, *103*, 103497. [CrossRef]
14. Shangxian, Y.; Haopeng, M.; Shuangbin, Q. Failure analysis of deep coal seam floor considering strain softening of surrounding rock and formation contact in goaf. *Coal Geol. Explor.* **2022**, *50*, 13.
15. Wu, J. Progressproblems and prospects of prevention and control technology of mine water and reutilization in China. *J. China Coal Soc.* **2014**, *39*, 795–805.
16. Shi, L.; Zhang, R.; Xu, D.; Li, Y.; Qiu, M.; Gao, W. Prediction of water inrush from floor based on GWO-Elman neural network. *J. China Coal Soc.* **2020**, *45*, 2455–2463.
17. Zhang, Y.; Yang, L. A novel dynamic predictive method of water inrush from coal floor based on gated recurrent unit model. *Nat. Hazards* **2021**, *105*, 2027–2043. [CrossRef]
18. Zhao, C.; Wang, X.; Ren, J.; Hao, J.; Meng, J. Prediction of water inrush risk from coal seam floor based on deep learning theory. *Chin. J. Undergr. Space Eng.* **2023**, *19*, 2090–2100.
19. Yin, S.; Xu, W.; Yin, H.; Cao, M. Study on risk assessment method of water inrush from thick floor aquifuge in deep mining. *Coal Sci. Technol.* **2020**, *48*, 83–89. [CrossRef]
20. Zhao, B.; Wang, Y.; Zhao, S.; Lü, K.; Su, Z.; Li, J. Mechanism and Prevention and Control Technology of Mine Earthquake in Fully Mechanized Top Coal Caving Face in Extra Thick Seam: Taking Longwanggou Coal Mine as an Example. *Sci. Technol. Eng.* **2023**, *23*, 12451–12457.
21. Li, C.; Zhang, Y.; Zuo, J.; Tang, S.; Liu, S. Floor failure mechanical behavior and partition characteristics under the disturbance of voussoir beam instability in deep coal mining. *J. China Coal Soc.* **2019**, *44*, 1508–1520.
22. Xue, W.; Wang, S.; Huang, K.; Ji, R.; Liu, M.; Ren, Y.; Xi, X.; Wang, F. Theoretical analysis and field measurement of floor failure in gob side entry of cutting roof in confined water mine area. *J. China Coal Soc.* **2020**, *45*, 581–588.
23. Xiaorong, H. Calculation of Coulomb's Earth Pressure Based on Triple Shear Failure Criterion. *HIghway* **2010**, *1*, 18–22.
24. Song, Z.; Hao, J.; Shi, Y.; Tang, J.; Liu, j. An overview of connotation and development of practical ground pressure contorl theory. *J. Shandong Univ. Sci. Technol. Nat. Sci.* **2019**, *38*, 1–15. [CrossRef]
25. Guo, H.b.; Chen, J.; Yang, S.; Zheng, H. The Selection Method for Tobacco Company Best Production Plan Based on Fuzzy Predictability Linear Programming Model and Improved Gray Cluster Analysis Theory. *Sci. Technol. Rev.* **2012**, *30*, 48–56.
26. Liu, Q.-Y.; Zhong, Z.-D.; Xu, R. Application of Rough Sets and Grey Clustering in Frequency of Wireless Railway Systems. In Proceedings of the 2010 6th International Conference on Wireless Communications Networking and Mobile Computing (WiCOM), Chengdu, China, 23–25 September 2010.
27. Liu, S.; Cai, H.; Cao, Y.; Yang, Y. Advance in grey incidence analysis modelling. In Proceedings of the 2011 IEEE International Conference on Systems, Man, and Cybernetics, Anchorage, AK, USA, 9–12 October 2011.
28. Zhang, K. Research on Degree of Grey Incidences Modeling Technology for Matrix Data. Ph.D. Thesis, Nanjing University of Aeronautics and Astronautics, Nanjing, China, 2010.
29. Wu, Q.; Zhang, Z.L.; Zhang, S.Y.; Ma, J.F. A new practical methodology of the coal floor water bursting II: The application of AHP vulnerable index method based on GIS. *J. Coal Sci.* **2007**, *32*, 1121–1126.
30. Wu, Q.; Wang, J.-H.; Liu, D.-H.; Cui, F.-P.; Liu, S.-Q. A new practical methodology of the coal floor water bursting evaluating IV: The application of AHP vulnerable index method based on GIS. *Mei T'an Hsueh Pao (J. China Coal Soc.)* **2009**, *2*, 233–238.
31. Yu, W.; Xie, J.; Ma, L.; Zhao, W.; Zhou, X. The water inrush risk assessment of roof of seam 13-1 in Xieqiao mine based on GIS and AHP. *Coal Geol. Explor.* **2016**, *44*, 69–73.
32. Ma, L.; Qian, J.; Zhao, W.; Zhou, X. GIS-based decision-making support system for prevention and control of water hazards in coal mines. *Coal Geol. Explor.* **2014**, *42*, 44–49.
33. Guo, X.; Shi, L. Research on quantitative analysis of water inrush through risk based on fault impact factor and fault fractal dimension characteristics. *J. Shandong Univ.* **2014**, *44*, 58–64.
34. Dai, G.; Xue, X.; Xu, K.; Niu, C.; Yang, T. Risk assessment of water inrush of No. 11 coal seam floor in Hancheng mining area on the basis of vulnerability index method. *Coal Geol. Explor.* **2017**, *45*, 112–117, 125.
35. Zhou, K.; Wang, B.Q. The evaluation of equivalent thickness of water-resisting layer. *Coal Chem. Ind.* **2016**, *39*, 45–47+51.

36. Shi, L.; Xu, D.; Qiu, M.; Jing, X.; Sun, H. Improved on the formula about the depth of damaged floor in working area. *J. China Coal Soc.* **2013**, *38*, 299–303.
37. Oti, E.U.; Olusola, M.O.; Eze, F.C.; Enogwe, S.U. Comprehensive review of K-Means clustering algorithms. *Criterion* **2021**, *12*, 22–23. [CrossRef]
38. Ashabi, A.; Sahibuddin, S.B.; Salkhordeh Haghighi, M. The systematic review of K-means clustering algorithm. In Proceedings of the 2020 9th International Conference on Networks, Communication and Computing, Tokyo, Japan, 18–20 December 2020.
39. Kushawah, Y.S.; Yadav, A.M. A survey on unsupervised clustering algorithm based on k-means clustering. *Int. J. Comput. Appl.* **2016**, *975*, 8887.
40. Wind, Y.; Saaty, T.L. Marketing applications of the analytic hierarchy process. *Manag. Sci.* **1980**, *26*, 641–658. [CrossRef]